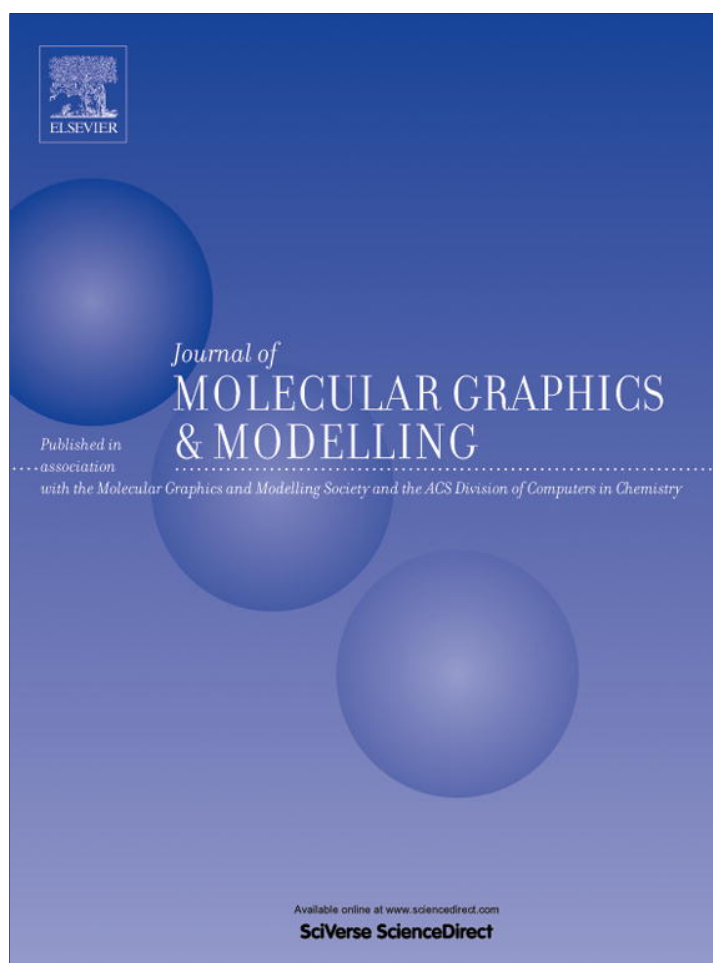


Provided for non-commercial research and education use.
Not for reproduction, distribution or commercial use.



(This is a sample cover image for this issue. The actual cover is not yet available at this time.)

This article appeared in a journal published by Elsevier. The attached copy is furnished to the author for internal non-commercial research and education use, including for instruction at the authors institution and sharing with colleagues.

Other uses, including reproduction and distribution, or selling or licensing copies, or posting to personal, institutional or third party websites are prohibited.

In most cases authors are permitted to post their version of the article (e.g. in Word or Tex form) to their personal website or institutional repository. Authors requiring further information regarding Elsevier's archiving and manuscript policies are encouraged to visit:

<http://www.elsevier.com/copyright>



Contents lists available at SciVerse ScienceDirect

Journal of Molecular Graphics and Modelling

journal homepage: www.elsevier.com/locate/JMGM

Extensive ligand-based modeling and in silico screening reveal nanomolar inducible nitric oxide synthase (iNOS) inhibitors

Ghadeer A.R.Y. Suaifan, Mayyada Shehadehh, Hebah Al-Ijel, Mutasem O. Taha*

Department of Pharmaceutical Sciences, Faculty of Pharmacy, University of Jordan, Amman, Jordan

ARTICLE INFO

Article history:

Received 26 December 2011
Received in revised form 20 February 2012
Accepted 2 April 2012
Available online 13 April 2012

Keywords:

Inducible nitric oxide synthase
Pharmacophore modeling
Quantitative structure–activity relationship
In silico screening

ABSTRACT

Inducible nitric oxide synthase (iNOS) has been implicated in a variety of diseases prompting several attempts to discover and optimize new iNOS inhibitors. Accordingly, we explored the pharmacophoric space of 143 iNOS inhibitors. Subsequently, genetic algorithm and multiple linear regression analysis were employed to select an optimal combination of pharmacophoric models and 2D physicochemical descriptors to produce self-consistent quantitative structure–activity relationship (QSAR) of optimal predictive potential (correlation coefficient $r_{115} = 0.83$, $F = 23.92$, $r_{LOO}^2 = 0.61$, r_{PRESS}^2 against 28 external test inhibitors = 0.51). Two orthogonal pharmacophores emerged in the QSAR equation suggesting the existence of at least two binding modes accessible to ligands within iNOS binding pocket. The pharmacophores were validated by comparison with crystallographic complexes of active iNOS inhibitors and receiver operating characteristic (ROC) curves analysis. We employed the pharmacophoric models and associated QSAR equation to screen the national cancer institute list of compounds (NCI). Three low nanomolar inhibitors were identified. The most potent hit exhibited irreversible inhibition of iNOS with IC_{50} value of 1.4 nM.

© 2012 Elsevier Inc. All rights reserved.

1. Introduction

Nitric oxide synthases (NOS) comprise a family of isozymes that catalyzes the oxidation of the natural substrate, L-arginine (L-Arg) to L-citrulline and nitric oxide (NO) [1]. Each NOS is active as a homodimer with each monomer containing C-terminal reductase domain and N-terminal oxygenase domain containing heme prosthetic group [2]. The substrate L-arginine and a redox cofactor, (6R)-5,6,7,8-tetrahydro-L-biopterin (H_4B), bind near the heme center in the oxygenase domain [3].

Nitric oxide (NO) is a double-edged sword molecule, beneficial as a messenger or modulator for immunological self-defense but at the same time, potentially toxic upon excessive production [4–6]. Classically, three distinct isoforms of NOS have been

identified and characterized as products of different genes with different subcellular localization, regulation, catalytic properties, and inhibitor sensitivities: endothelial and neuronal NOSs (eNOS and nNOS, respectively) are expressed constitutively in the vascular endothelium and nervous system, respectively. Neuronal NO acts as a neurotransmitter [7], while endothelial NO regulates the blood pressure and the vascular tone [8]. On the other hand, NO generated by the third isoform, i.e., inducible NOS (iNOS), plays an important role in the regulation of immune reactions [9,10].

The fact that excessive stimulation of iNOS is implicated in several pathological conditions such as rheumatoid arthritis [8], colitis [11], cancer [12], tissue damage and cell apoptosis following inflammation [8], prompted continuous interest to develop a bewildering array of new iNOS inhibitors [8]. These can be classified into substrate (i.e., L-arginine) or non-amino acid-based inhibitors [8]. However, although some iNOS inhibitors have been investigated in clinical trials [8], none reached the market because of some major limitations, including: toxicity, lack of selectivity and poor bioavailability and cellular penetration [13–15]. These limitations leave the door wide open for continuous efforts toward the discovery of new iNOS inhibitors.

The main focus of recent efforts toward the development of new iNOS inhibitors concentrate on structure-based ligand design [16–20], e.g., de novo design/docking [8], and high throughput screening [8]. Structure-based design efforts were fueled by the availability of satisfactory crystallographic structures for iNOS. To date, several iNOS X-ray complexes are documented in the Protein

Abbreviations: AUC, area under the curve; ACC, overall accuracy; DMSO, dimethyl sulfoxide; eNOS, endothelial nitric oxide; FN, false negative; FNR, overall false negative rate; FP, false positive; FPR, overall false positive rate; HBD, hydrogen bond donor; HBA, hydrogen bond acceptor; Hbic, hydrophobic; iNOS, inducible nitric oxide; MS, mass spectroscopy; NMR, nuclear magnetic radiation; nNOS, neuronal nitric oxide; PDB, protein data bank; QSAR, quantitative structure–activity relation; r_{BS}^2 , bootstrapping regression coefficient; r_{LOO}^2 , leave one out correlation coefficient; r_{PRESS}^2 , predictive r^2 for external set; ROC, receiver operating characteristic curve analysis; Se, sensitivity; Sp, specificity; SPC, overall specificity; TN, true negative; TP, true positive; TPR, overall true positive rate; VS, virtual screen.

* Corresponding author. Tel.: +962 6 5355000x23305; fax: +962 6 5339649.

E-mail address: mutasem@ju.edu.jo (M.O. Taha).

Data Bank (e.g., PDB codes: 3NOS, 3E67, 3E68, 3E7G, 3E7T [21], 2ORS, 1DD7 [22], 4NOS with resolution range: 2.0–2.6 Å). However, although considered the most reliable structural information that can be used for drug design, crystallographic structures are limited by inadequate resolution [23] and crystallization-related artifacts of the ligand–protein complex [24–26]. Moreover, crystallographic structures generally ignore structural heterogeneity related to protein anisotropic motion and discrete conformational substrates [27]. Incidentally, iNOS has been shown via molecular dynamics simulations (MD) to exhibit significant induced fit flexibility upon binding to different ligands [28].

The continued interest in designing new iNOS inhibitors and lack of adequate ligand-based computer-aided drug discovery efforts combined with the drawbacks of structure-based design and the significant induced fit flexibility observed for iNOS [28] prompted us to explore the possibility of developing ligand-based three-dimensional (3D) pharmacophore(s) integrated within self-consistent QSAR model. This approach avoids the drawbacks of structure-based techniques; furthermore, the pharmacophore model(s) can be used as 3D search query(ies) to discover new iNOS inhibitory scaffolds. We previously reported the use of this innovative approach toward the discovery of new inhibitory leads against glycogen synthase kinase-3 β [29], bacterial MurF [30], protein tyrosine phosphatase [31], DPP IV [32], hormone sensitive lipase [33], β -secretase [34], influenza neuraminidase [35], cholesteryl ester transfer protein [36], CDK1 inhibitors [37], and HSP90 inhibitors [38].

We employed the HYPOGEN module from the CATALYST software package [39] to construct plausible binding hypotheses for a diverse list of iNOS inhibitors. Subsequently, genetic function algorithm (GFA) and multiple linear regression (MLR) analyses were employed to search for an optimal QSAR that combine high-quality binding pharmacophores with other molecular descriptors capable of explaining bioactivity variation across a collection of diverse iNOS inhibitors. The optimal pharmacophores were subsequently used as 3D search queries to screen the national cancer institute (NCI) list of compounds for new iNOS inhibitory leads.

2. Experimental

2.1. Molecular modeling

2.1.1. Software and hardware

The following software packages were utilized in the present research.

- CATALYST (Version 4.11), Accelrys Inc. (www.accelrys.com), USA.
- CERIOUS2 (Version 4.10), Accelrys Inc. (www.accelrys.com), USA.
- CS ChemDraw Ultra 6.0, Cambridge Soft Corp. (<http://www.cambridgesoft.com>), USA.
- Discovery Studio 2.5, Accelrys Inc. (www.accelrys.com), USA.

Pharmacophore and QSAR modeling studies were performed using CATALYST (HYPOGEN module) and CERIOUS2 software suites from Accelrys Inc. (San Diego, California, www.accelrys.com) installed on a Silicon Graphics Octane2 desktop workstation equipped with a dual 600 MHz MIPS R14000 processor (1.0 GB RAM) running the Irix 6.5 operating system. Structure drawing was performed employing ChemDraw Ultra 6.0 which was installed on a Pentium 4 PC.

2.1.2. Data set

The structures of 143 iNOS inhibitors (1–143, Table 1) were collected from recently published literature [20,40–52]. Although the *in vitro* bioactivities of the collected inhibitors were

gathered from separate articles they were determined employing the same bioassay methodologies. The bioactivities were expressed by their inhibition constant K_i (μM). The logarithm of measured K_i (μM) values were used in the three-dimensional quantitative structure–activity analysis (3D-QSAR) thus correlating the data linear to the free energy change.

The two-dimensional (2D) chemical structures of the inhibitors were sketched using ChemDraw Ultra and saved in MDL-molfile format. Subsequently, they were imported into CATALYST, converted into corresponding standard 3D structures and energy minimized to the closest local minimum using the molecular mechanics CHARMM force field implemented in CATALYST. The resulting 3D structures were utilized as starting conformers for CATALYST conformational analysis. It is worth mentioning that CATALYST automatically considers all possible protonation states of ionizable species during pharmacophore exploration thus exempting the need of pretreatment to account for different protonation states.

2.1.3. Conformational analysis

The molecular flexibilities of the collected compounds were taken into account by considering each compound as a collection of conformers representing different areas of the conformational space accessible to the molecule within a given energy range. Accordingly, the conformational space of each inhibitor (1–143, Table 1) was explored adopting the “best conformer generation” option within CATALYST based on the generalized CHARMM force field implemented in the program. Default parameters were employed in the conformation generation procedure of training compounds and screened library (NCI), i.e., a conformational ensemble was generated with an energy threshold of 20 kcal/mol from the local minimized structure at which has the lowest energy level and a maximum limit of 250 conformers per molecule [39].

2.1.4. Pharmacophoric hypotheses generation

All 143 molecules with their associated conformational models were regrouped into a spreadsheet. The biological data of the inhibitors were reported with an “Uncertainty” value of 3, which means that the actual bioactivity of a particular inhibitor is assumed to be situated somewhere in an interval ranging from one-third to three-times the reported bioactivity value of that inhibitor [53–56]. Subsequently, seven structurally diverse training subsets (sets I–VII in Table A under Supplementary Material) were carefully selected from the collection for pharmacophore modeling (See Section 3.1 for more details).

The selected training sets were utilized to conduct 51 modeling runs to explore the pharmacophoric space of iNOS inhibitors (Table B under Supplementary Material). The exploration process included altering interfeature spacing parameter (100 and 300 pm) and the maximum number of allowed features in the resulting pharmacophore hypotheses, i.e., they were allowed to vary from 4 to 5 or 5 to 5 with and without exclusion spheres (Table B under Supplementary Material). Pharmacophore modeling employing CATALYST proceeds through three successive phases: the constructive phase, subtractive phase and optimization phase (see CATALYST modeling Algorithm in SM-1 under Supplementary Materials) [8].

2.1.5. Assessment of the generated hypotheses

When generating hypotheses, CATALYST attempts to minimize a cost function consisting of three terms: Weight cost, Error cost and Configuration cost (see CATALYST cost analysis in Section SM-2 under Supplementary Materials) [39,53,54].

An additional approach to assess the quality of CATALYST-HYPOGEN pharmacophores by cross-validation using the Cat-Scramble program implemented in CATALYST was applied. This

Table 1
The structures of iNOS inhibitors utilized in modeling.

Compound	R ₁	R ₂	R ₃	R ₄	K _i (μM)	Ref ^a
1		H	H	H	161	[51]
2		H	H	H	238	[51]
3		H	H	H	297	[51]
4		H	H	H	195	[51]
5		H	H	H	200	[51]
6 ^b		H	H	H	174	[51]
7		H	H	H	425	[51]
8		H	H	H	222	[51]
9 ^b		CH ₃	H	CH ₃	56.6	[51]
10		H	H	CH ₃	8.95	[51]

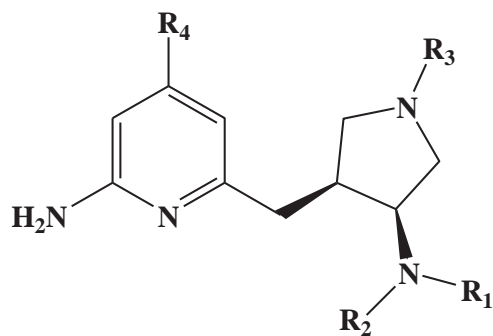
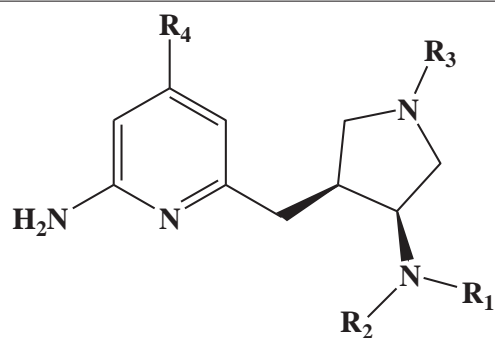


Table 1 (Continued)



Compound	R ₁	R ₂	R ₃	R ₄	K _i (μM)	Ref ^a
11		H	H	CH ₃	9.48	[51]
12		H	H	CH ₃	14.1	[51]
13		H	H	CH ₃	7.97	[51]
14		H	H	CH ₃	13.6	[51]
15		H	H	CH ₃	9.01	[51]
16		H	H	CH ₃	3.56	[51]
17		H	H	CH ₃	7.7	[51]
18		H	H	CH ₃	5.4	[51]
19		H	H	CH ₃	4.6	[51]

Table 1 (Continued)

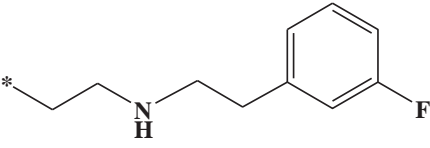
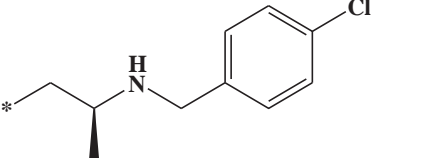
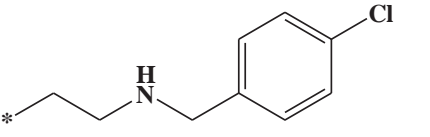
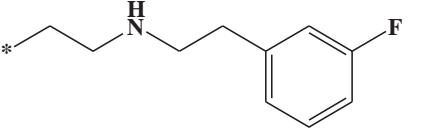

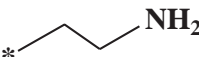
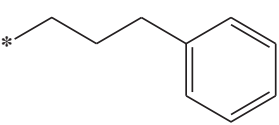
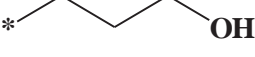
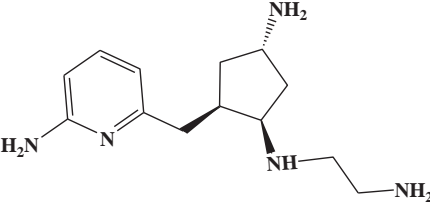
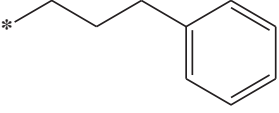
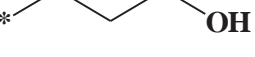
20 ^b		H	H	CH ₃	4.06	[51]
21		H	H	CH ₃	12.2	[51]
22 ^b		CH ₃	H	CH ₃	22.8	[51]
23		CH ₃	H	CH ₃	38.2	[51]
24 ^b		H	H	CH ₃	5.84	[51]
25		H	H	H	58.4	[50]
26		H	H	H	166.2	[50]
27		H	H	H	143.1	[50]
28					51.9	[50]
29		H	Benzyl	H	609.4	[50]
30		H	Benzyl	H	2523	[50]

Table 1 (Continued)

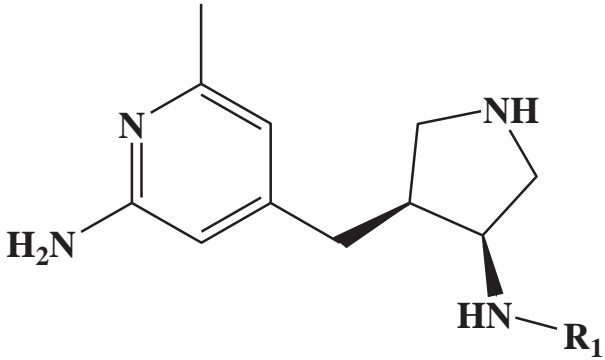
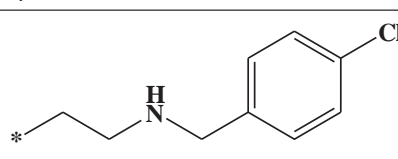
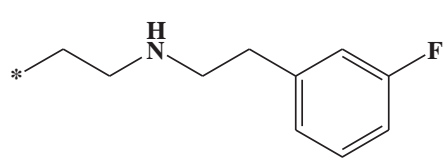
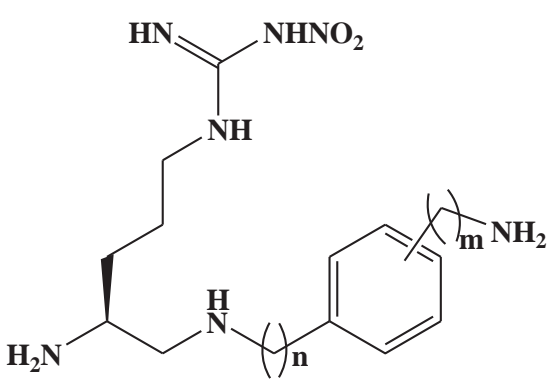
			
Compound	R ₁	K _i (μM)	Ref ^a
31		232	[51]
32 ^b		10.6	[51]
			
Compound	<i>n, m</i>	K _i (μM)	Ref ^a
33	<i>n</i> = 0, <i>m</i> = 0, <i>meta</i>	279	[46]
34	<i>n</i> = 0, <i>m</i> = 0, <i>para</i>	339	[46]
35	<i>n</i> = 1, <i>m</i> = 0, <i>ortho</i>	86.3	[46]
36	<i>n</i> = 1, <i>m</i> = 0, <i>meta</i>	572	[46]
37 ^b	<i>n</i> = 1, <i>m</i> = 0, <i>para</i>	326	[46]
38	<i>n</i> = 2, <i>m</i> = 0, <i>ortho</i>	184	[46]
39	<i>n</i> = 2, <i>m</i> = 0, <i>meta</i>	166	[46]
40	<i>n</i> = 2, <i>m</i> = 0, <i>para</i>	339	[46]
41 ^b	<i>n</i> = 0, <i>m</i> = 1, <i>ortho</i>	29.3	[46]
42	<i>n</i> = 0, <i>m</i> = 1, <i>meta</i>	80	[46]
43	<i>n</i> = 0, <i>m</i> = 1, <i>para</i>	335	[46]
44	<i>n</i> = 0, <i>m</i> = 2, <i>ortho</i>	3.51	[46]
45 ^b	<i>n</i> = 0, <i>m</i> = 2, <i>meta</i>	260	[46]
46 ^b	<i>n</i> = 0, <i>m</i> = 2, <i>para</i>	360	[46]

Table 1 (Continued)

Compound	n	R ₁	R ₂	K _i (μM)	Ref ^a
47 ^b	1		H	154	[46]
48	1		H	141	[46]
49	1		H	392	[46]
50 ^b	2		H	72.6	[46]
51	2		H	178	[46]
52	2		H	395	[46]
53	4	NH ₂	H	123	[47]
54	3	NH ₂	H	73	[47]
55 ^b	2	NH ₂	H	39	[47]
56	2	NH ₂	OH	31	[52]
57	2	NH ₂	NH ₂	72	[52]
58	2	OH	H	391	[49]
59	3	OH	H	853	[49]
60	4	OH	H	318	[49]

Table 1 (Continued)

Compound	R ₁	R ₂	R ₃	K _i (μM)	Ref ^a
61		H	H	29	[47]
62		H	H	200	[47]
63		OH	H	31	[52]
64		H	H	108	[20]
65		H	H	112	[20]
66		H	H	176	[20]
67		H	H	1049	[20]
68 ^b		H	H	396	[20]
69 ^b		H	CH ₃	127	[20]
70		H	CH ₃	243	[20]
71 ^b		H	CH ₃	475	[20]
72		H	CH ₃	1010	[20]

Table 1 (Continued)

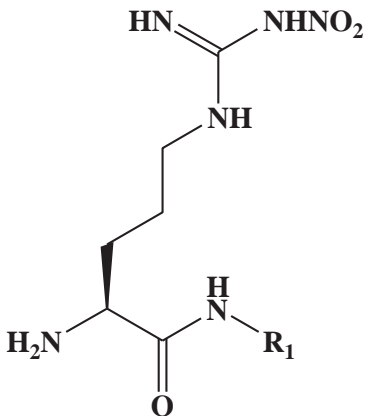
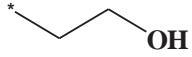
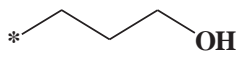
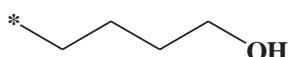
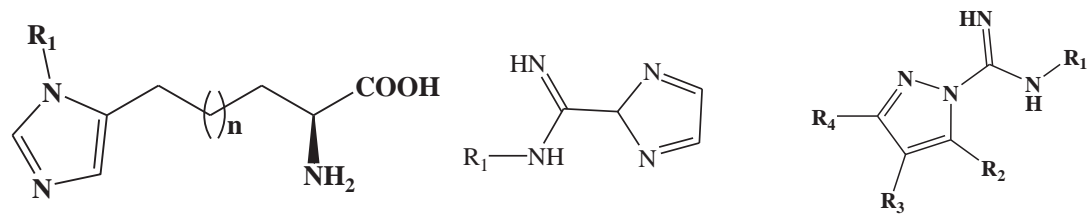
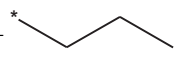
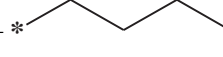
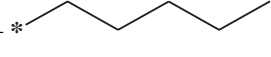
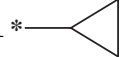
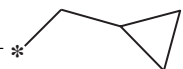
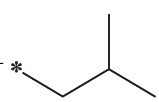
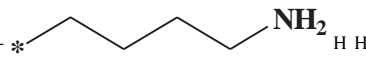
						
Compound	R ₁	K _i (μM)	Ref ^a			
73		181	[49]			
74 ^b		645	[49]			
75		373	[49]			
						
Compound	Scaffold	n R ₁	R ₂ R ₃	R ₄	K _i (μM)	Ref ^a
76	A	0H	--	-	950	[43]
77	A	1H	--	-	10	[43]
78	A	2H	--	-	35	[43]
79	A	3H	--	-	8	[43]
80	A	4H	--	-	40	[43]
81	A	1Ph	--	-	100	[43]
82	A	2Ph	--	-	50	[43]
83	A	3Ph	--	-	120	[43]
84 ^b	B	-H	--	-	0.7	[45]
85	B		--	-	5	[45]
86	B		--	-	14	[45]
87 ^b	B		--	-	50	[45]
88	B		--	-	80	[45]
89	B		--	-	22	[45]
90	B		--	-	150	[45]
91	C		H H	H	50	[45]

Table 1 (Continued)

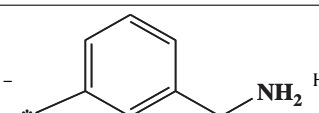
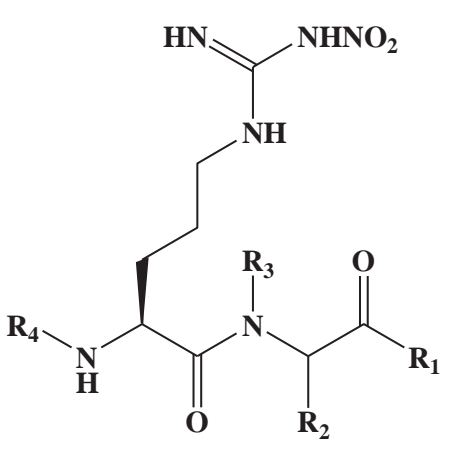
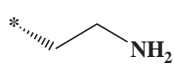
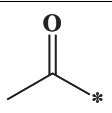
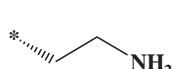
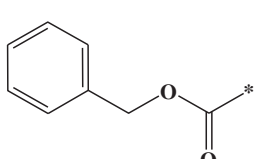
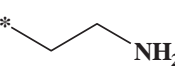
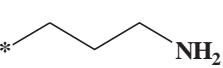
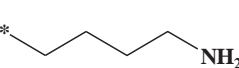
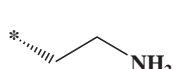
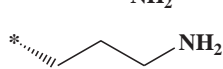
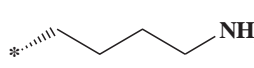
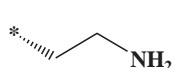
A		B		C		R ₄	Ki (μM)	Ref ^a
Compound Scaffold		n	R ₁	R ₂	R ₃			
92	C	-		H	H	H	12	[45]
93	C	-H	-H	H	H	CH ₃	9	[45]
94	C	-H	-H	H	CH ₃	H	3	[45]
95	C	-H	-H	CH ₃	H	CH ₃	750	[45]
								
Compound	R ₁	R ₂	R ₃	R ₄		Ki (μM)	Ref ^a	
96	NH ₂		H			2600	[44]	
97 ^b	NH ₂		H			1600	[44]	
98	NH ₂	H		H		760	[44]	
99	NH ₂	H		H		1000	[44]	
100 ^b	NH ₂	H		H		1100	[44]	
101	NH ₂		CH ₃	H		340	[44]	
102	NH ₂		CH ₃	H		1300	[44]	
103	NH ₂		CH ₃	H		1900	[44]	
104	OCH ₃		H	H		27	[44]	

Table 1 (Continued)

Compound	R1	R2	R3	R4	Ki (μM)	Ref ^a
105	OC(CH ₃) ₃		H	H	413	[44]
106	OH		H	H	1210	[44]
107	NH ₂		H	H	25	[42]
108	NH ₂		H	H	61	[42]

Compound	Name	Ki (μM)	Ref ^a
109	L-Arg ^{NO2} -L-Phe	160	[40]
110	L-Phe-L-Arg ^{NO2}	93	[40]
111	L-Arg ^{NO2} -L-Phe-OMe	45	[40]
112^b	L-Phe-L-Arg ^{NO2} -OMe	204	[40]
113	L-Arg ^{NO2} -L-Phe-OBn	18	[40]
114	L-Phe-L-Arg ^{NO2} -OBn	45	[40]
115	L-Arg ^{NO2} -D-Phe-OMe	100	[40]
116	D-Arg ^{NO2} -L-Phe-OMe	6400	[40]
117	D-Arg ^{NO2} -D-Phe-OMe	6500	[40]
118	D-Arg ^{NO2} -L-Phe-OMe	7500	[40]
119	L-Arg ^{NO2} -D-Phe-OMe	1200	[40]
120	D-Arg ^{NO2} -D-Phe-OMe	3600	[40]
121^b	D-Phe-D-Arg ^{NO2}	13,600	[40]
122	L-Arg ^{NO2} -L-Arg ^{NO2} -NH ₂	62	[42]
123^b	L-Arg ^{NO2} -D-Asn-NH ₂	8.9	[42]
124	D-Arg ^{NO2} -L-Ser-NH ₂	1180	[42]
125	L-Arg ^{NO2} -D-Orn-NH ₂	103	[42]
126^b	L-Arg ^{NO2} -L-Lys-NH ₂	104	[42]
127	L-Arg ^{NO2} -L-Orn-NH ₂	97	[42]
128^b	L-Lys-D-Arg ^{NO2} -NH ₂	4700	[42]
129^b	D-Lys-D-Arg ^{NO2} -NH ₂	910	[42]
130	D-Phe-D-Arg ^{NO2} -NH ₂	13,600	[47]

Compound	Name	Ki (μM)	Ref ^a
131		50	[20]
132		140	[20]

Table 1 (Continued)

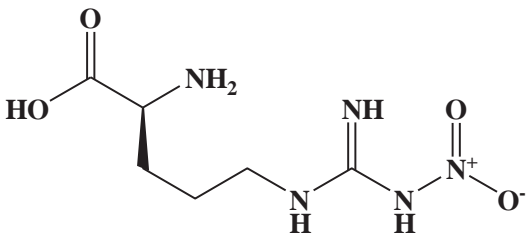
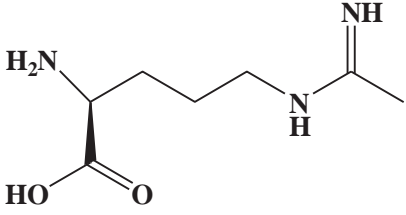
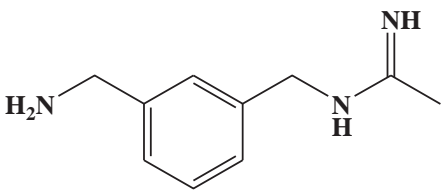
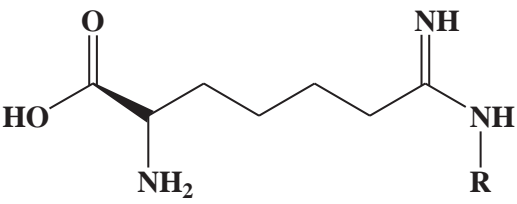
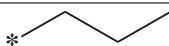
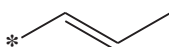

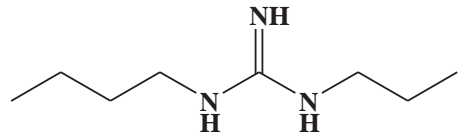
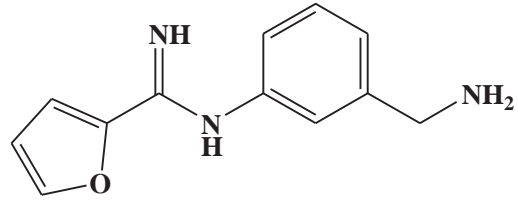
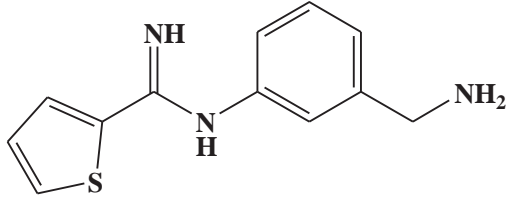
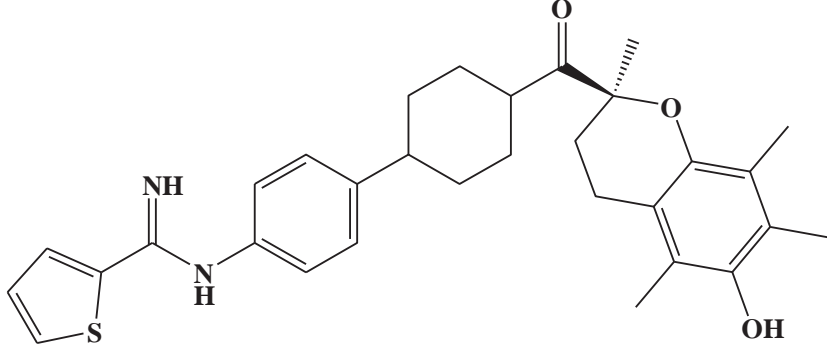
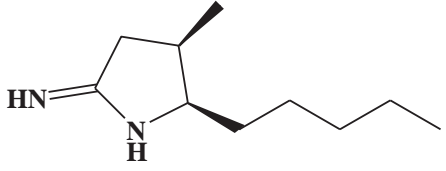
Compound	Name	Ki (μM)	Ref ^a
133		8	[52]
134 ^b		13.7	[48]
135		23.8	[48]
			
Compound	R	Ki (μM)	Ref ^a
136	* 	180	[41]
137	* 	2.1	[41]
138	* 	0.62	[41]
Compound	Structure	Ki (μM)	Ref ^a
139		780	[43]
140		0.16	[43]

Table 1 (Continued)

Compound	Structure	K _i (μM)	Ref ^a
141		0.12	[43]
142		>300	[47]
143		0.25	[47]

*Connection point.

^a Reference number in the article.^b These compounds were employed as the external testing subset in QSAR modeling.

validation procedure is based on Fisher's randomization test [57]. In this validation test; we selected a 95% confidence level, which instruct CATALYST to generate 19 random spreadsheets by the Cat-Scramble command. Subsequently, CATALYST-HYPOGEN is challenged to use these random spreadsheets to generate hypotheses using exactly the same features and parameters used in generating the initial unscrambled hypotheses. Success in generating pharmacophores of comparable cost criteria to those produced by the original unscrambled data reduces the confidence in the training compounds and the unscrambled original pharmacophore models [39,57,58]. Based on Fisher randomization criteria; only 367 pharmacophores exceeded the 85% significance threshold for subsequent processing (clustering and QSAR analyses).

2.1.6. Clustering of the generated pharmacophore hypotheses

The successful models (367) were clustered into 121 (one representative from close sets of 3 models) groups utilizing the hierarchical average linkage method available in CATALYST. Subsequently, the highest-ranking representatives, as judged based on their significance *F*-values, were selected to represent their corresponding clusters in subsequent QSAR modeling. Table C under Supplementary Material shows information about representative pharmacophores including their pharmacophoric features, success criteria and differences from corresponding null hypotheses. The table also shows the corresponding Cat. Scramble confidence levels for each representative pharmacophore.

2.1.7. QSAR modeling

A subset of 115 compounds from the total list of inhibitors (1–143, Table 1) was utilized as a training set for QSAR modeling; the remaining 28 molecules (ca. 20% of the dataset) were employed as an external test subset for validating the QSAR models. The test molecules were selected as follows: the 143 inhibitors were ranked according to their *K_i* values, and then every fifth compound was selected for the test set starting from the high-potency end. The selected test inhibitors are marked with double asterisks in Table 1.

The logarithm of measured 1/*K_i* (μM) values was used in QSAR, thus correlating the data linear to the free energy change. The chemical structures of the inhibitors were imported into CERIU2 as standard 3D single conformer representations in SD format. Subsequently, different descriptor groups were calculated for each compound employing the C2.DESRIPTOR module of CERIU2. The calculated descriptors included various simple and valence connectivity indices, electro-topological state indices and other molecular descriptors (e.g., logarithm of partition coefficient, polarizability, dipole moment, molecular volume, molecular weight, molecular surface area, etc.) [59]. The training compounds were fitted (using the best-fit option in CATALYST) against the representative pharmacophores (121 models, Table 1 and Table D under Supplementary Materials), and their fit values were added as additional descriptors. The fit value for any compound is obtained automatically via Eq. (D) under Supplementary Materials [39]. Genetic function approximation (GFA) was employed to search for the best possible QSAR regression equation [59] (see Section SM-3 under Supplementary Materials).

Our preliminary diagnostic trials suggested the following optimal GFA parameters: explore linear, quadratic and spline equations at mating and mutation probabilities of 50%; population size = 500; number of genetic iterations = 30,000 and lack-of-fit (LOF) smoothness parameter = 1.0. However, to determine the optimal number of explanatory terms (QSAR descriptors), it was decided to scan and evaluate all possible QSAR models resulting from 4 to 17 explanatory terms.

All QSAR models were validated employing leave one-out cross-validation (r_{LOO}^2), bootstrapping (r_{BS}^2) and predictive r^2 (r_{PRESS}^2) calculated from the test subsets. The predictive r_{PRESS}^2 is defined as in Eq. (1):

$$r_{\text{PRESS}}^2 = \frac{\text{SD} - \text{PRESS}}{\text{SD}} \quad (1)$$

where SD is the sum of the squared deviations between the biological activities of the test set and the mean activity of the training set molecules, PRESS is the squared deviations between predicted and actual activity values for every molecule in the test set.

2.1.8. In silico screening for new iNOS inhibitors

Two pharmacophoric models emerged in the optimal QSAR equation namely; **HypoIII/18/9** and **HypoV/31/5** (see Section 3). Accordingly these models were employed as 3D search queries to screen the NCI 3D flexible structural database. Screening was performed employing the “Best Flexible Database Search” option implemented within CATALYST. Hits were filtered according to Lipinski’s [60] and Veber’s [61] rules. Remaining hits were fitted against the two pharmacophores using the “best fit” option within CATALYST. The fit values together with the relevant molecular descriptors of each hit were substituted in the optimal QSAR equation (2). The highest ranking molecules based on QSAR predictions were acquired and tested in vitro.

2.2. In vitro experimental studies

2.2.1. Materials

All of the chemicals used in these experiments were purchased from Sigma–Aldrich (Germany). NCI samples were kindly provided by the National Cancer Institute. Potent hits of $\geq 70\%$ inhibition at $100 \mu\text{M}$ were assessed for their IC_{50} values and were found to be $\geq 95\%$ purity based on CHN elemental analysis (see Table G and Figs. D–I under Supplementary Materials, that show the NMR and MS spectrums of most active hits). Murine macrophage iNOS were purchased from Sigma–Aldrich (St. Louis, MO, USA), water for bioanalysis (Sigma, St. Louis, MO, USA), DMSO for bioanalysis (Sigma, St. Louis, MO, USA).

2.2.2. Preparation of hit compounds for in vitro assay

The tested compounds were provided as dry powders. They were initially dissolved in DMSO to give stock solutions of $100 \mu\text{M}$. Subsequently, they were diluted to the required concentrations with HEPES buffer pH 7.4 for enzymatic assay.

2.2.3. Quantification of iNOS activity by hemoglobin capture assay

Nitric oxide formation from NOS was monitored by the hemoglobin capture assay as described earlier [62] despite some modifications. Briefly, each bioassay was performed by mixing the tested compound solution (100 , 10 , 1 , and $0.1 \mu\text{M}$) with iNOS enzyme (ca. $30 \mu\text{g}$), L-arginine ($10 \mu\text{L}$, 2mM), hemoglobin- A_0 ($10 \mu\text{L}$, 1mM), tetrahydrobiopterin ($1 \mu\text{L}$, 1mM) and Dithio-DL-threitol ($10 \mu\text{L}$, 10mM) in HEPES (100mM , pH 7.4) to a final volume of 1mL and the reaction was initiated by addition of NADPH ($10 \mu\text{L}$, 15mM). The rate of NO production was monitored by subtracting the change of absorbance at 421nm over five

minutes from the change of absorbance at 401nm on a Perkin-Elmer Lambda 10 UV/vis spectrophotometer (see Figs. B2 and B3 under Supplementary Materials show the typical spectrophotometric recording and analysis for the inhibitory activity of hit 145 as an example) [72]. The percentage of residual activity of NOS was determined for each compound by comparing the activity with NOS enzyme under the same experimental conditions and without the presence of any inhibitor (negative control). The inhibitory activity of L- N^G -monomethyl Arginine (L-NMMA, 144 in Table 5) was determined under the same experimental conditions as standard inhibitor (positive control). The IC_{50} values were obtained from the dose-dependent inhibition plots. Figs. A–C under Supplementary Materials show the dose–response curves of the potent hits (**145**, **153** and **158**). All assays were performed at room temperature and all the inhibitors were preincubated with enzyme for five minute at room temperature prior to reaction initiation.

3. Results and discussion

3.1. Ligand-based modeling

CATALYST-HYPOGEN models drug-receptor interaction using information derived from the ligands. HYPOGEN identifies a 3D array of a maximum of five chemical features common to active training molecules (i.e., pharmacophores), which provides a relative alignment for each input molecule consistent with their binding to a proposed common receptor site. In fact, CATALYST pharmacophores (binding hypotheses) explain the variability of bioactivity with respect to the geometric localization of the chemical features present in the molecules used to build it. The chemical features considered can be hydrogen bond donors and acceptors (HBds and HBAs), aliphatic and aromatic hydrophobes (Hbic), positive and negative ionizable (Poslon and Neglon) groups. The conformational flexibility of training ligands is modeled by creating multiple conformers, sensibly calculated to emphasize representative coverage over a specified energy range (see Section 2.1.3). CATALYST pharmacophores have been used as 3D queries for database searching and in 3D-QSAR studies [39].

A total of 143 compounds were used in this study (Table 1) [20,40–52]. The fact that pharmacophore modeling requires limited number of carefully selected training compounds (from 16 to 45 compounds only) [56] of bioactivity variations attributable solely to the presence or absence of pharmacophoric features, i.e., not due to steric or electronic factors, makes it impossible to explore the pharmacophore space of large training sets in one shot, partly because CATALYST-HYPOGEN is not suited to handle large number of compounds and partly because pharmacophore modeling is generally confused by electronic and steric bioactivity modifying factors commonly encountered in SAR data. This dilemma prompted us to break the collected compounds into smaller training subsets compatible with pharmacophore modeling, i.e., of bioactivity variations attributable solely to the presence or absence of pharmacophoric features (3D SAR). Nevertheless, the basic problem in this approach is to identify a particular training set capable of representing the whole list of collected compounds. This problem can be very significant in cases of large SAR lists, as in our case. We found that the best way to solve this problem is by exploring the pharmacophoric space of several carefully selected training subsets, i.e., from the whole list of collected compounds, followed by allowing the resulting pharmacophores to compete within the context of GFA-QSAR analysis such that the best pharmacophore(s) that are capable of explaining bioactivity variations across the whole list of collected compounds is(are) selected. However, since pharmacophore models fail in explaining electronic and steric bioactivity-modulating effects, the GFA-QSAR process should be allowed to select other 2D

Table 2

Pharmacophoric features, corresponding tolerances and 3D coordinates (X, Y, Z) of optimal iNOS based pharmacophore models.

Model ^a	Definitions	Chemical features						
			HBD ^c		Hbic ^d	Hbic	PosIons ^e	
HypoIII/18/9^g	Weights		2.21059		2.21059	2.21059	2.21059	
	Tolerances ^b		1.60		1.60	1.60	1.60	
	Coordinates	X	0.39	3.32	2.16	-2.08	0.58	
		Y	2.41	2.06	-1.98	1.02	-2.15	
		Z	2.19	2.76	1.70	-0.74	-1.90	
	HBA ^f		HBD		Hbic	Hbic	PosIons	
HypoV/31/5	Weights		2.71818		2.71818	2.71818	2.71818	
	Tolerances		1.60		1.60	1.60	1.60	
	Coordinates	X	-3.61	-6.18	4.31	1.84	0.98	-2.78
		Y	0.50	-0.98	-0.70	-1.40	0.74	1.94
		Z	-1.68	-1.01	1.95	3.54	1.20	-2.04

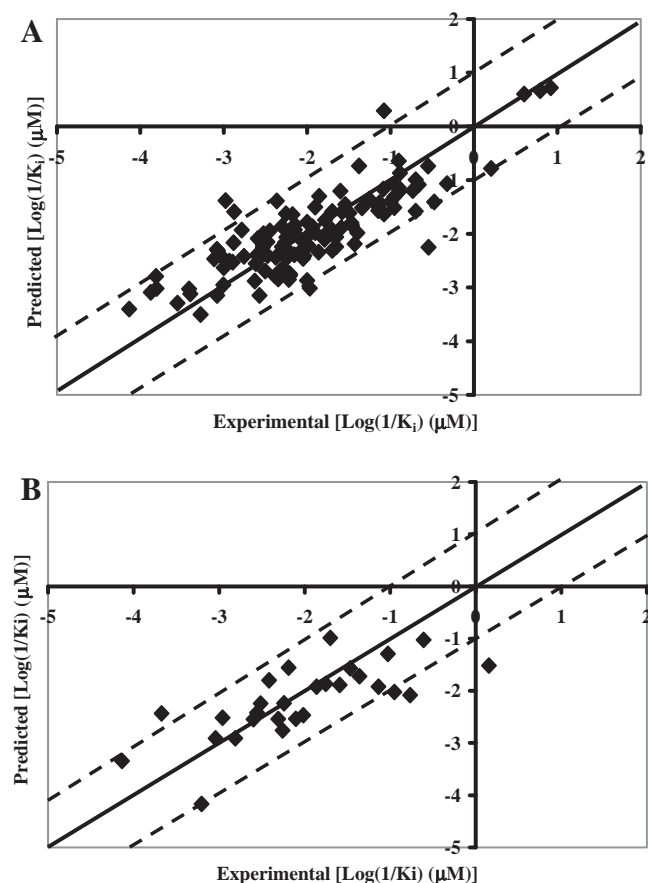
^a Pharmacophoric hypothesis shown in Figs. 2 and 3.^b Tolerances: refer to the radius of feature spheres (Å).^c HBD: hydrogen bond donor feature.^d Hbic: hydrophobic feature.^e PosIons: positive ionizable.^f HBA: hydrogen bond acceptor feature.^g Number of exclusion spheres in **HypoIII/18/9** = 10 of 1.2 Å tolerance, at the following X,Y, Z coordinates: (-0.28, -4.14, 2.03), (-4.35, -3.05, -1.41), (10.35, 3.09, 0.87), (3.96, 2.00, 6.21), (-5.31, -0.79, 5.15), (0.08, -1.11, -5.34).

Fig. 1. Experimental versus (A) fitted (115 compounds, $r_{LOO}^2 = 0.61$) and (B) predicted (28 compounds, $r_{PRESS}^2 = 0.51$) bioactivities calculated from the best QSAR model Eq. (2). The solid lines are the regression lines for the fitted and predicted bioactivities of training and test compounds, respectively, whereas the dotted lines indicate 1.0 log point error margins.

physicochemical descriptors to complement the selected pharmacophore(s).

Accordingly, seven training subsets were selected from the collection (subsets I–VII, Table A under Supplementary Material). Each subset consisted of inhibitors of maximal 3D diversity that

appear to follow certain 3D structure–activity relationship (SAR) rule [53,54]. Pharmacophore exploration of these subsets yielded 121 plausible binding models (see Sections 2.1.4–2.1.6 and Sections SM-1–SM-4, and Tables A and B under Supplementary Materials).

Subsequently, we employed QSAR analysis to search for the best combination of pharmacophore(s) (among the best 121 models) and other 2D descriptors [59] capable of explaining bioactivity variation across the whole list of collected inhibitors (1–143, Table 1). We employed genetic function approximation and multiple linear regression QSAR (GFA-MLR-QSAR) analysis to search for an optimal QSAR equation (see Section 2.1.7) [29–38,59,63].

Eq. (2) shows the details of the optimal QSAR model. Fig. 1 shows the corresponding scatter plots of experimental versus estimated bioactivities for the training and testing inhibitors. $\text{Log}(1/K_i) = -3.06 + 1.72 [\text{HypoIII}/18/9 - 7.65] + 9.21 \times 10^{-2} [\text{HypoV}/31/5 - 5.02] - 1.41 \times 10^{-2} (\kappa^{\alpha})^2 + 28.30 [\text{SdssC} - 0.64] + 1.73 [\text{JursFPSA2} - 2.57] + 0.66 [\text{HBA} - 1] + 2.15 \times 10^{-2} \text{HBD2} + 0.53 [\text{AlogP98} + 1.81] + 1.64 [\text{AtypeC25} - 1] - 2.20 [\text{AtypeC25} - 2]$

$$r_{115} = 0.83, F\text{-statistic} = 23.92, r_{bs}^2 = 0.69, r_{LOO}^2 = 0.61,$$

$$r_{PRESS}^2 = 0.51 \quad (2)$$

where, r_{115} is the correlation coefficient against 115 training compounds, r_{LOO}^2 is the leave-one-out correlation coefficient, r_{bs}^2 is the bootstrapping regression coefficient and r_{PRESS}^2 is the predictive r^2 determined for 28 external testing compounds [59,63].

HypoIII/18/9 and **HypoV/31/5** represent the fit values of training compounds (calculated using Eq. D, Section SM-2 under Supplementary Materials) against the 9th and 5th pharmacophoric models generated from 18th and 31st CATALYST runs employing the training subsets III and V, respectively (bolded models in Table C under Supplementary Materials). Figs. 2–6 show the two pharmacophores and how they map various iNOS inhibitors.

HBA and HBD are the number of hydrogen-bond acceptors and donors, respectively; AlogP98 is logarithmic transformation of the partition coefficient. AtypeC25 is one of the thermodynamic AlogP.Atypes family of descriptors and it encodes for the summation of phenyl rings and aromatic methyl groups (including CF₃), κ_1^{α} is Kier's first order alpha-modified shape index encoding for molecular branching through count of atoms and presence of cycles relative to minimal and maximal graphs, JursFPSA2 is the fractional negatively charged partial surface area obtained by dividing partial

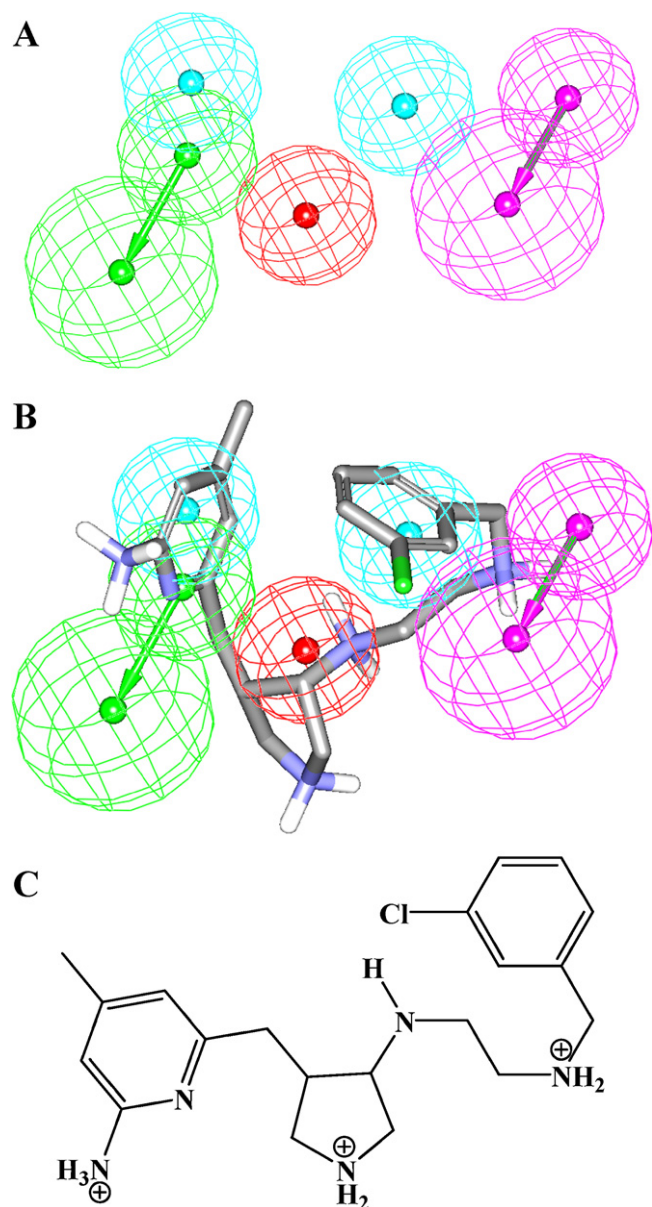


Fig. 2. (A) Pharmacophoric features of **HypoV/31/5**. HBA as green vectored spheres, HBD as pink vectored spheres, Hbic as blue spheres, Poslon as red spheres (B) **HypoV/31/5** fitted against 11 ($K_i=9.48 \mu\text{M}$, Table 1), and (C) chemical structure of 11. (For interpretation of the references to color in this figure legend, the reader is referred to the web version of the article.)

negative surface area (sum of the solvent-accessible surface areas of all negatively charged atoms) by the total molecular solvent accessible surface area. Finally, SdssC encodes for the electrotopological state index of $=\text{C}$ carbon atoms [59]. Tables D and E, under Supplementary Materials, show the numerical values of descriptors in the optimal QSAR model (Eq. (2)) calculated for training and testing compounds, respectively.

Noticeably, several descriptors emerged in Eq. (2) in spline format. The spline terms employed herein are “truncated power splines” and are denoted by bolded brackets ($\{\}$). For example, $\{f(x) - a\}$ equals zero if the value of $(f(x) - a)$ is negative; otherwise, it equals to $(f(x) - a)$ [59].

Interestingly, emergence of **HypoIII/18/9** and **HypoV/31/5** in Eq. (2) suggests they represent two complementary binding modes accessible to ligands within the binding pocket of iNOS, i.e., one explains the bioactivities of certain group of iNOS inhibitors, while

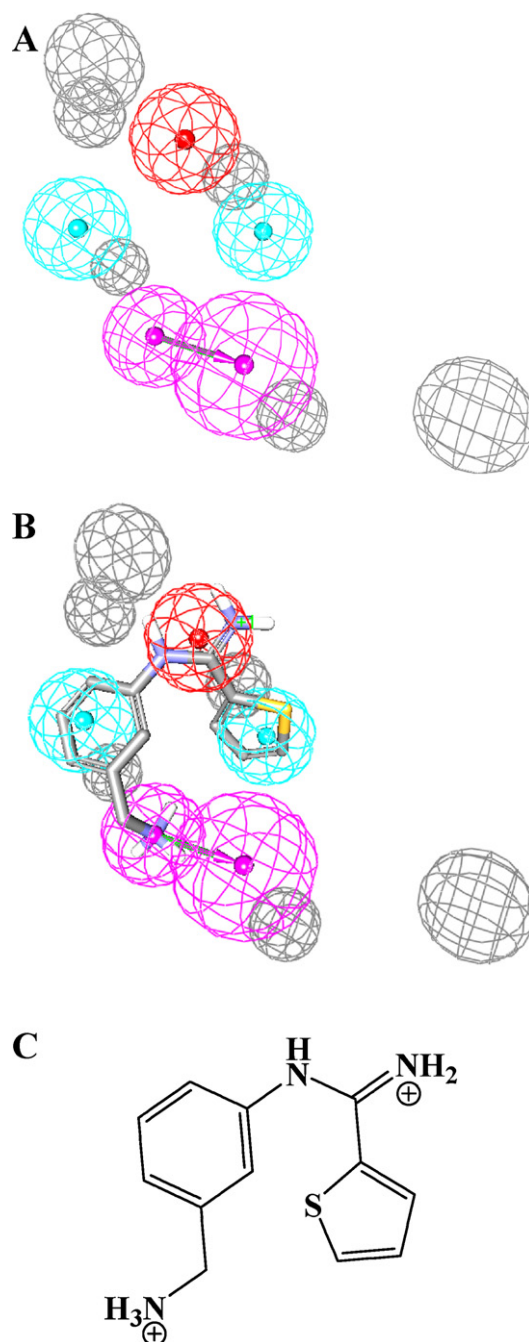


Fig. 3. (A) Pharmacophoric features of **HypoIII/18/9**. HBD as pink vectored spheres, Hbic as blue spheres, Poslon as red spheres (B) **HypoIII/18/9** fitted against 141 ($K_i=0.12 \mu\text{M}$, Table 1), (C) chemical structure of 141. (For interpretation of the references to color in this figure legend, the reader is referred to the web version of the article.)

the other explains the bioactivities of the rest. Table 2 shows the X, Y, and Z coordinates of the two pharmacophores. Both **HypoIII/18/9** and **HypoV/31/5** appeared in Eq. (2) in spline format, indicating that each binding mode will only contribute to ligand/iNOS affinity if the fit value of the particular ligand exceeds the corresponding spline threshold. For example, the ability of a certain ligand to map **HypoIII/18/9** will impact its actual affinity to iNOS only if its respective fit value exceeds 7.65 (the spline intercept associated with this pharmacophore in Eq. (2)), which is a fairly high value particularly knowing that the maximum fit value is 10. In other words, ligand binding to iNOS is sensitive to correct alignment among

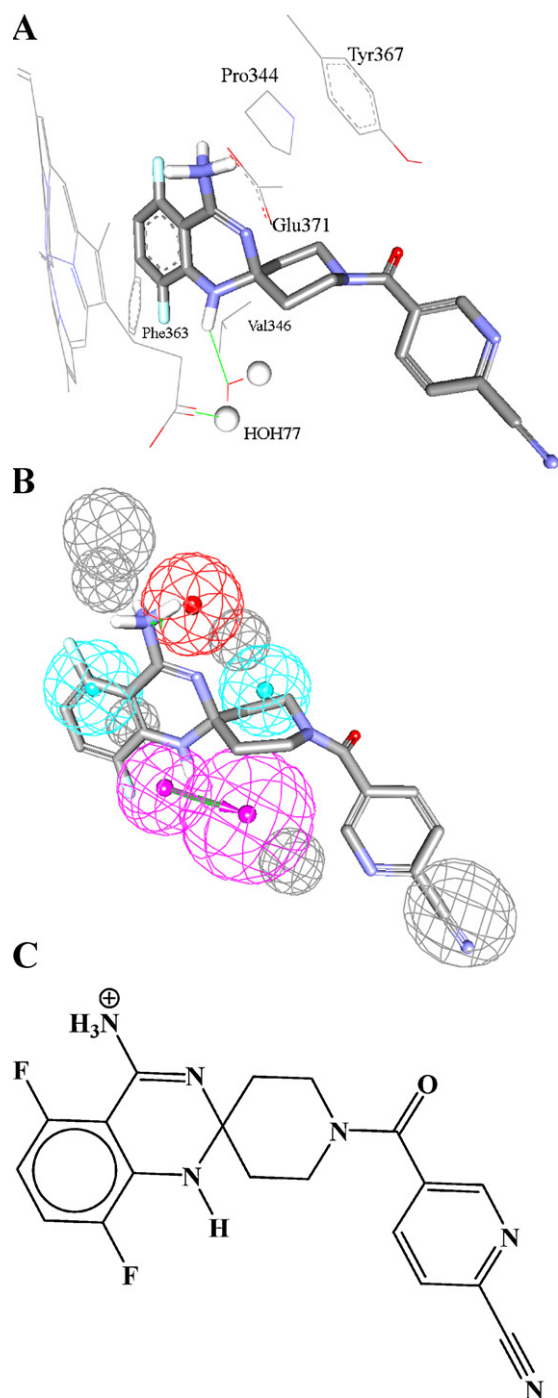


Fig. 4. (A) Co-crystallized ligand of iNOS (PDB code: 3E7T, resolution 2.6 Å), (B) **HypoIII/18/9** mapped against the co-crystallized ligand of 3E7T, and (C) the chemical structure of the co-crystallized ligand of 3E7T.

Table 3
Performance of QSAR-selected pharmacophores as 3D search queries.

Pharmacophore model	ROC ^a –AUC ^b	ACC ^c	SPC ^d	TPR ^e	FNR ^f
HypoIII/18/9	0.97	0.97	0.98	0.48	0.017
HypoV/31/5	0.98	0.97	0.99	0.16	0.0056

^a Receiver operating characteristic.

^b Area under the curve.

^c Overall accuracy.

^d Overall specificity.

^e Overall true positive rate.

^f Overall false negative rate.

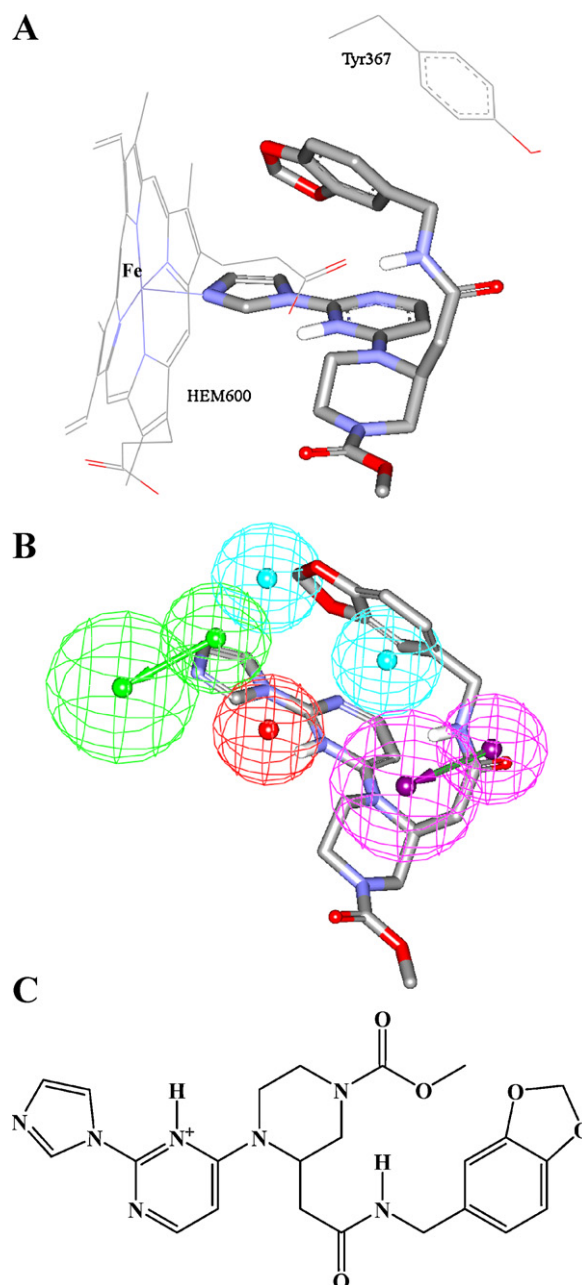


Fig. 5. (A) Co-crystallized ligand of iNOS (PDB code: 1DD7, resolution 2.25 Å), (B) **HypoV/31/5** mapped against the co-crystallized ligand of 1DD7, and (C) the chemical structure of the co-crystallized ligand of 1DD7.

complementary groups within ligand–iNOS complex. Still, the two models succeeded significantly in separating active iNOS inhibitors from decoys upon testing by receiver-operating (ROC) curve analysis [57–60] with ROC – AUC values of 97% to 98%, respectively, as

Table 4
The number of captured compounds by each pharmacophore model.

3D database	Post screening filtering ^b	Pharmacophore models	
		HypoV/31/5	HypoIII/18/9
NCI ^a	Before	4539	11,751
	After	1661	5039

^a NCI: national cancer institute list of available compounds (238,819 structures).

^b Using Lipinski's and Veber's rules. One Lipinski's violations were tolerated.

shown in Table 3 and Fig. 7 (see Section SM-4 under Supplementary Materials for more details) [57,58,60,66–69].

Emergence of topological and shape descriptors (i.e., κ_1^α and SdssC) in Eq. (2) illustrates certain role played by the ligands' topology in the binding process. However, despite the predictive significance of these descriptors, their information content is obscure.

On the other hand, emergence of JursFPSA2 in Eq. (2) combined with positive regression coefficient, suggests a direct relationship between ligand/iNOS affinity and ligands' negative charges. We believe this trend is explainable by the fact that iNOS binding is mediated, at least partially, by ionic attraction involving negatively charged ligand groups and a positively charged region within iNOS binding site [61], which we believe is the guanidino of Arg193.

Moreover, the contradictory emergence of HBA, HBD, and AlogP98 combined with positive regression coefficients, i.e., bioactivity is directly related to hydrophilic and hydrophobic ligand properties exemplified by HBA/HBD and LogP, respectively,

suggests that ligand–iNOS binding achieves maximal values at certain optimal ligand hydrophilic/hydrophobic balance. Excessive hydrophilicity such that AlogP becomes ≤ 1.81 nullifies any positive contributions from Log P to binding. On the other hand, extreme hydrophobic ligand properties can adversely influence HBA and HBD contributions to affinity.

Finally, judging from the regression coefficients of different descriptors in Eq. (2) and descriptors' ranges across all training compounds (see Table D under Supplementary Materials), **HypoIII/18/9** is the second most prominent contributor to bioactivity next to SdssC with maximum contributions to bioactivity of 15.2 and 20.9 log cycles, respectively. On the other hand, the analysis shows that HBD and **HypoV/31/5** are the least influential with maximum contributions to bioactivity of 2.6 and 1.2 log cycles, respectively. However, the remaining descriptors, namely, $(\kappa_1^\alpha)^2$, AtypeC25, JursFPSA2, HBA, and AlogP98 have moderate contributions to bioactivity as reflected by their maximal bioactivity enhancements of 9.4, 8.2, 7.0, 5.9 and 4.0 log cycles, respectively.

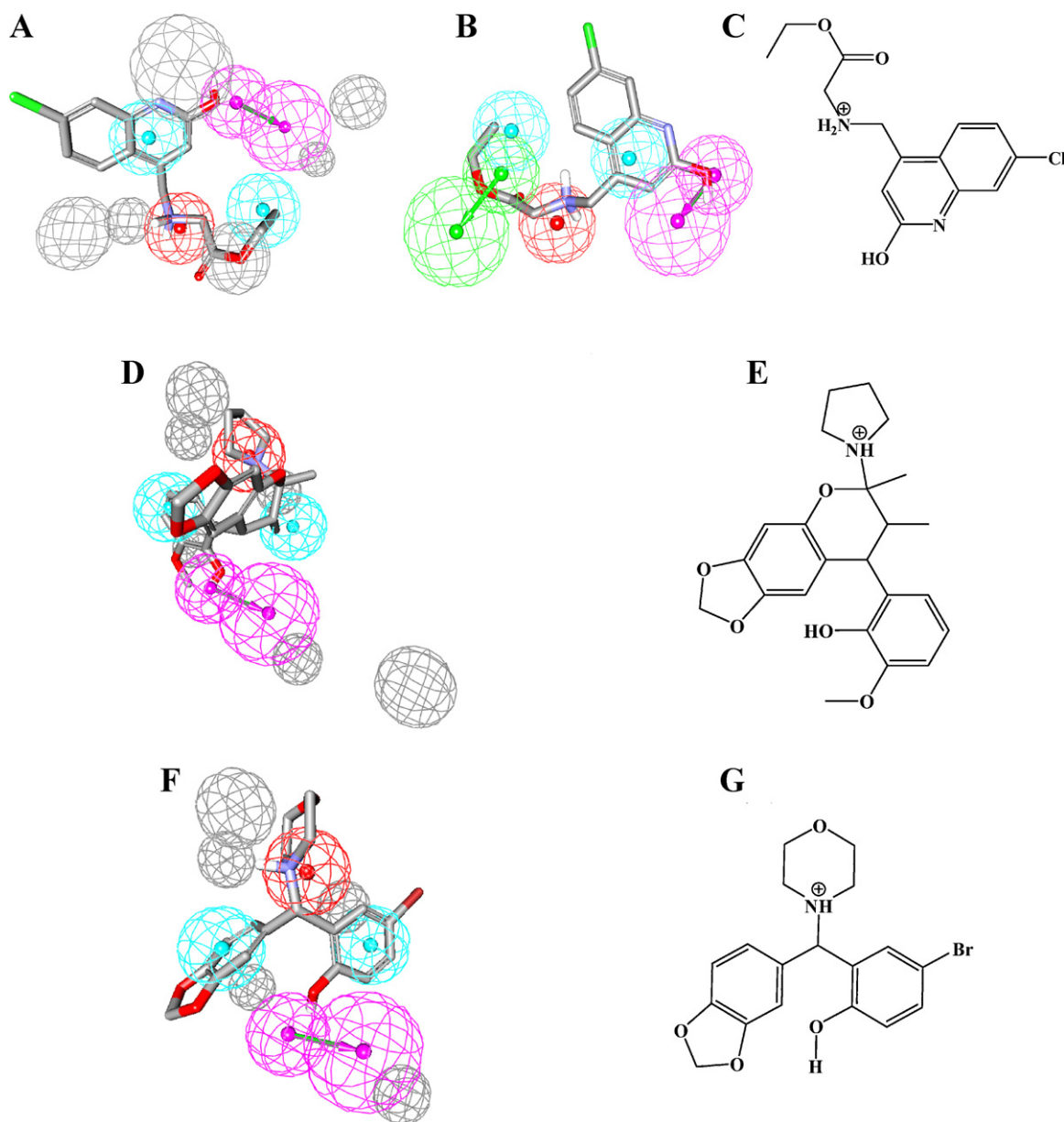


Fig. 6. (A) and (B) Mapping hit 145 (IC₅₀ = 1.4 nM, Table 5) against **HypoIII/18/9** and **HypoV/31/5**, respectively. (D) and (F) Fitting **HypoIII/18/9** against hits 153 (IC₅₀ = 45 nM, Table 5) and 158 (IC₅₀ = 63 nM, Table 5), respectively. (C), (E) and (G) are the 2D structures of 145, 153 and 158, respectively.

Accordingly, one can conclude that **HypoIII/18/9** is the dominant contributor to bioactivity compared to **HypoV/31/5**.

3.2. Comparison of pharmacophore model with the active site of iNOS

To further emphasize the validity of our pharmacophore/QSAR modeling approach, we compared the pharmacophoric features of **HypoIII/18/9** with the way it maps a co-crystallized ligand within iNOS ($IC_{50} = 35$ nM, PDB code: 3E7T) [21], as in Fig. 4. Mapping the cyclic NH of the co-crystallized ligand against HBD in **HypoIII/18/9** (Fig. 4B) corresponds to hydrogen bonding interactions tying this NH with one of the carboxylate side chains of heme via bridging H_2O molecule (Fig. 4A). Similarly, mapping the difluorobenzene ring of the co-crystallized ligand against one of the hydrophobic features in **HypoIII/18/9** (Fig. 4B) corresponds to introducing this ring into a hydrophobic pocket comprised of the heme ring system, the aromatic side chain of Phe363 and the hydrophobic side chain of Val346 (Fig. 4A). Another hydrophobic interaction can be seen between the ethylene of the piperidine central ring of the co-crystallized ligand and cycloalkyl fragment of Pro344, as shown in Fig. 4A. This interaction is represented by mapping the ethylene fragment of the piperidine of the ligand against hydrophobic feature in **HypoIII/18/9** (Fig. 4B). Finally, mapping the amidine group of the co-crystallized ligand against Poslon feature in **HypoIII/18/9** (Fig. 4B) correlates with electrostatic attraction connecting this group with the carboxylate of Glu371 in the co-crystallized complex (Fig. 4A).

A similar analogy can be seen upon comparing the crystallographic structure of another co-crystallized ligand within iNOS protein ($K_i = 2.2$ nM, PDB code: 1DD7) [22] with the way it maps **HypoV/31/5**. Fig. 5 compares the chemical structure of the co-crystallized ligand and how it maps **HypoV/31/5** employing rigid mapping, i.e., fitting the ligand's bound state against the pharmacophore without conformational adjustments. Clearly, mapping the amidic NH of the co-crystallized ligand against HBD feature in **HypoV/31/5** (Fig. 5B) corresponds to hydrogen bonding interactions tying this NH with one of the carboxylate side chains in the heme cofactor (Fig. 5A). Similarly, mapping the benzo[1,3]dioxole fragment of the ligand against two hydrophobic features in **HypoV/31/5** (Fig. 5B) corresponds to π stacking and hydrophobic interactions against the aromatic ring of Tyr367 and one of the pyrrole components of the heme cofactor, respectively (Fig. 5A). Fitting the guanidine nucleus of the co-crystallized ligand against Poslon feature in **HypoV/31/5** (Fig. 5B) seems to correlate with electrostatic attraction tying this group with the two carboxylate side chains of the heme structure (Fig. 5A). Finally, fitting the imidazole nitrogen of the co-crystallized ligand against HBA feature in **HypoV/31/5** (Fig. 5B) agrees with the formation of coordinate bond between this nitrogen and the iron core of the heme prosthetic group (Fig. 5A).

Clearly from the above discussion, **HypoIII/18/9** and **HypoV/31/5** represent two valid binding modes assumed by ligands within iNOS. However, despite that the two models share 4 features (2 Hbics, Poslon, and HBD) they differ in the 3D distribution of their features, particularly their HBDs (see Fig. 6A and B for comparison).

Interestingly, since 1DD7 complex represents iNOS-dimerization inhibitors [14], while 3E7T complex [13] represents iNOS enzymatic inhibitor, it can be suggested that the corresponding pharmacophores, i.e., **HypoV/31/5** and **HypoIII/18/9**, respectively, represent the binding requirements of iNOS dimerization and enzymatic inhibitors, respectively. Furthermore, the fact that iNOS enzymatic inhibitors are generally more potent than iNOS dimerization inhibitors correlates nicely with our QSAR-based (Eq. (2)) finding that **HypoIII/18/9** has superior influence on anti-iNOS bioactivity compared to **HypoV/31/5**.

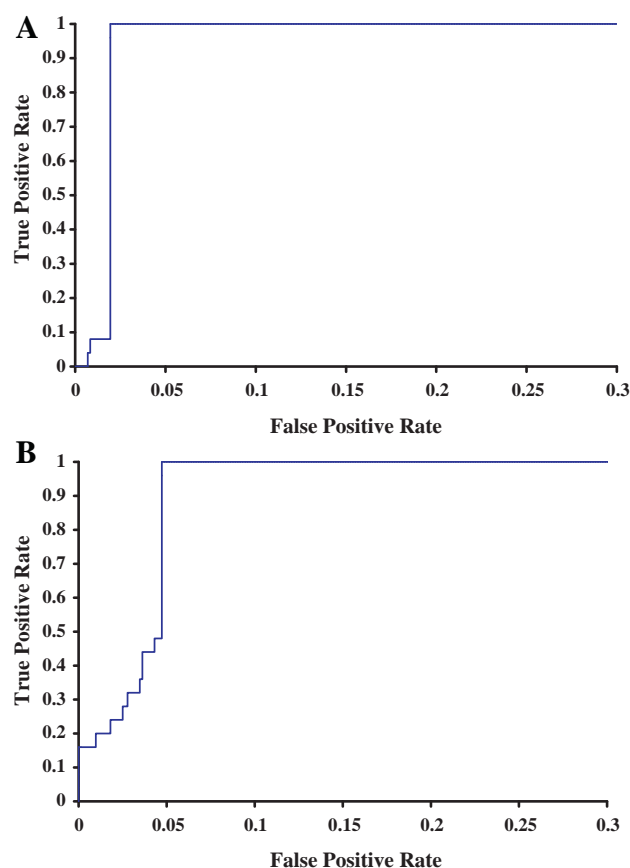


Fig. 7. ROC curves of: (A) **HypoV/31/5** and (B) **HypoIII/18/9**.

It remains to be mentioned, these models point to limited number of critical interactions required for high ligand–iNOS affinity in each of the binding modes. In contrast, crystallographic complexes reveal many bonding interactions without highlighting critical ones. Incidentally, Figs. 4A and 5A only show interactions corresponding to pharmacophoric features while other binding interactions were hidden for clarity.

3.3. In silico screening and subsequent in vitro evaluation

HypoIII/18/9 and **HypoV/31/5** were employed as 3D search queries against the NCI list of compounds (238,819 structures). Table 4 summarizes the numbers of captured hits by **HypoV/31/5** and **HypoIII/18/9**. Captured hits were subsequently filtered based on Lipinski's and Veber's rules [60,61].

Surviving hits were fitted against **HypoV/31/5** and **HypoIII/18/9** and their fit values, together with other relevant molecular descriptors, were substituted in QSAR equation (2) to predict their iNOS K_i values. The highest-ranking 14 available hits were evaluated in vitro against murine iNOS via an established hemoglobin capture assay that measures the amount of released NO [47,64,65,70,71]. Table F under Supplementary Materials shows the numerical values of QSAR descriptors (Eq. (2)) calculated for the highest-ranking hits, while Table 5 shows their corresponding predicted bioactivities.

Experimental bioassay commenced by screening hits at $100 \mu\text{M}$ concentrations, subsequently; active compounds of inhibition percentages $\geq 70\%$ were further assessed to determine their IC_{50} values. Table 5 shows the highest ranking acquired hits and their corresponding experimental anti-iNOS bioactivities.

We validated the bioassay procedure by evaluating the anti-iNOS IC_{50} of the standard inhibitor L-NMMA, which was found to

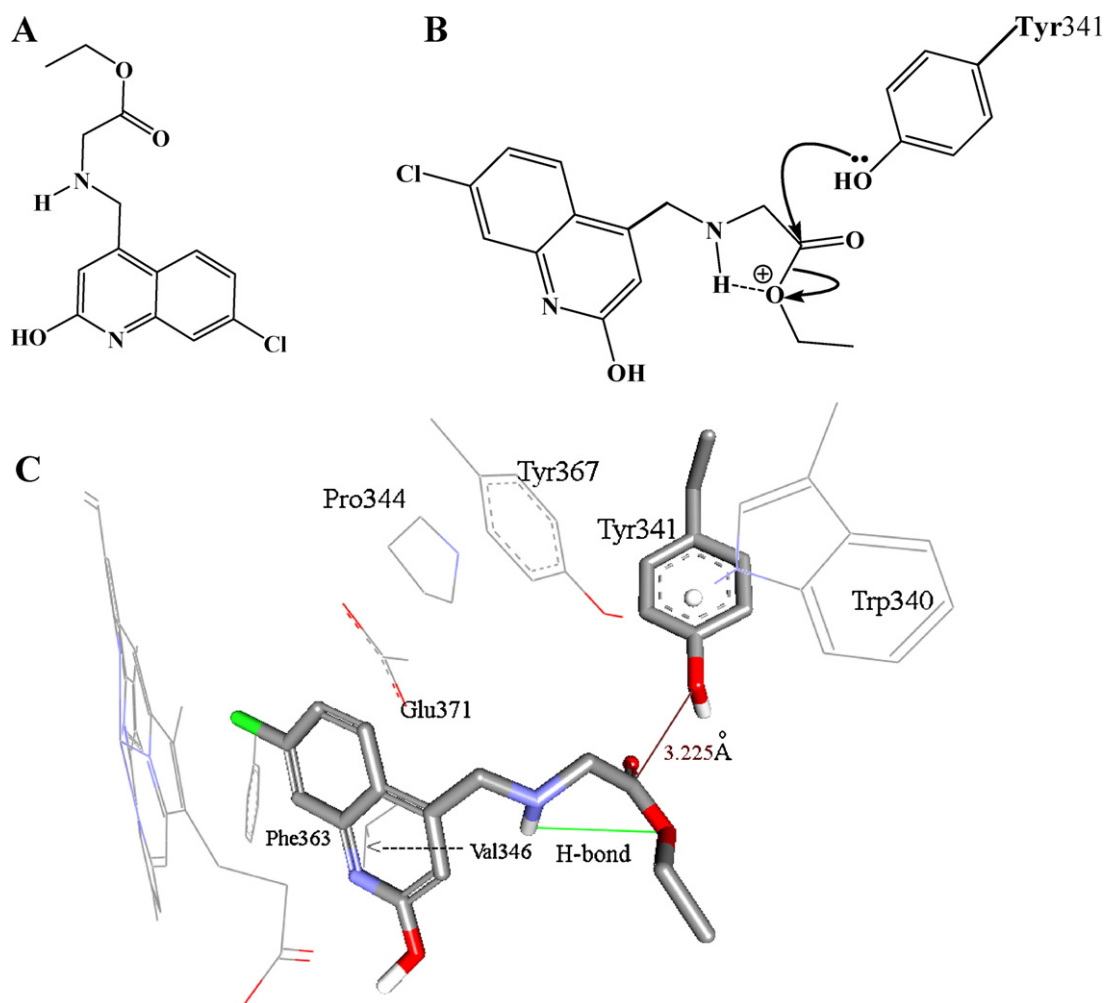


Fig. 8. (A) chemical structure of NCI hit 145 ($IC_{50} = 1.4$ nM), (B) proposed mechanism of covalent bond formation between the inter-molecularly hydrogen-bonded ester-side chain of 145 and the phenolic hydroxyl of Tyr341, and (C) docked pose of 145 into iNOS binding pocket (PDB code: 3E7T, resolution 2.6 Å) showing the close proximity between the phenolic hydroxyl of Tyr341 and the activated carboxylic carbonyl of 145.

be 8.66 μ M (see Table 5), which is close to the reported IC_{50} of this inhibitor (14.0 μ M, Fig. A in Supplementary Material) [41].

In vitro testing showed that the 14 high-ranking hits possess moderate to high inhibitory percentages against iNOS ranging from 30 to 87% (Table 5 and Figs. A–C in Supplementary Materials). However, hit 145 was the most potent with IC_{50} value of 1.4 nM, while the IC_{50} of hits **153** and **158** were 45 nM and 63 nM, respectively. Fig. 6 shows how our QSAR-selected pharmacophores fit **145**, **153**, and **158**. Interestingly, potent hits **153** and **158** fitted only **HypoIII/18/9**, while they didn't map **HypoV/31/5** as evident from Table 5 and Fig. 6. In fact, **HypoV/31/5** failed to map most of our tested hits (Table 5). This trend is not unexpected as the regression contribution of **HypoV/31/5** in QSAR equation (2) is only marginal (slope = 9.21×10^{-2}) compared to the dominate **HypoIII/18/9** (slope = 1.72).

It remains to be mentioned that although QSAR predictions of some hits were accurate, as exemplified in the IC_{50} values of potent hits **153** and **158** (Table 5), however, others were rather overestimated (e.g., 147, 148, 149 and 156, Table 5). We believe these prediction errors are attributable to two factors: (i) Minimal structural similarity between training compounds and captured hits, and (ii) extrapolation error: the fact that many of the captured hits were predicted to be of better bioactivities than all training compounds suggests certain degree in prediction error due to extrapolation. Tables D and F under Supplementary Materials show the values

of QSAR descriptors in Eq. (2) calculated for training compounds and captured hits, respectively. Clearly from the average values of descriptors in both tables, the two sets (training compounds and captured hits) differ significantly in 5 out of 9 descriptors of Eq. (2), namely, **HypoIII/18/9**, SdssC, HBD, AlogP98 and AtpcC25, which probably explains the observed extrapolatory overestimation of some hits. Paradoxically, their excellent predictions prompted us to select these particular hits for in vitro assessment.

Interestingly, hit compound 145 illustrated significantly higher potency than predicted by QSAR equation (2). Further evaluation of 145 unveiled an irreversible inhibitory profile against iNOS. This behavior was proved by monitoring the anti-iNOS activity of 145 upon dilution. 145 caused 87% inhibition at 100 μ M, however, upon 10-fold dilution in situ; the enzyme remained inhibited to the same extent suggesting irreversible bonding and inhibition of the enzyme. In contrast, in situ dilution of the reversible standard inhibitor L-NMMA caused reversible reduction of iNOS inhibition. We believe the irreversible inhibitory profile of 145 against iNOS is related to the existence of kinetically favorable hydrogen-bonded five-membered ring involving the amino-NH and the ester oxygen of the aliphatic side chain of 145. Hydrogen-bonding probably enhances the electrophilic character of the carboxylic ester carbonyl group, and therefore, promotes attacks by nucleophilic groups within the binding pocket. Fig. 8 details a strongly probable proposed mechanism for the irreversible inhibitory profile of

Table 5
High-ranking hit molecules with their fit values against **HypoIII/18/9** and **HypoV/31/5** their corresponding QSAR estimates from Eq. (2) and in vitro iNOS inhibitory activities.

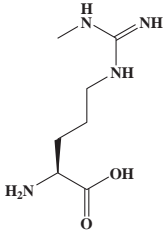
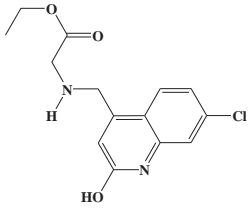
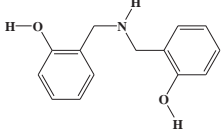
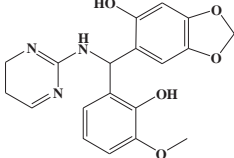
No. ^a	Name	Structure	Fit values ^b		QSAR Predictions ^c Ki (nM)	Experimental ^d		
			HypoIII/18/9	HypoV/31/5		% Inhibition at 100 μ M	IC ₅₀ (nM)	Ki (nM) ^e
144	L-NMMA-standard inhibitor		-	-	-	-	8.66 μ M $r^2 = 0.92^g$	1.1 μ M
145	NCI0346209		7.7	12.0	18	87 ^{g,f}	1.4 $r^2 = 0.98^g$	0.41
146	NCI0026194		7.3	10.3	184	57 ^f	-	-
147	NCI0667922		8.0	8.2	44	60 ^f	-	-

Table 5 (Continued)

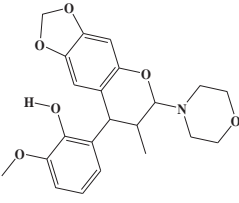
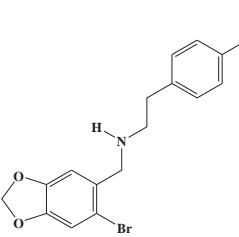
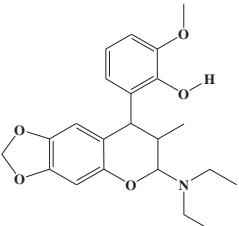
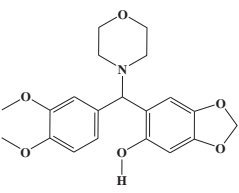
No. ^a	Name	Structure	Fit values ^b		QSAR Predictions ^c Ki (nM)	Experimental ^d		
			HypoIII/18/9	HypoV/31/5		% Inhibition at 100 μM	IC ₅₀ (nM)	Ki (nM) ^e
148	NCI0666214		8.3	0	44	73 ^f	-	-
149	NCI0154572		7.4	9.5	53	64 ^f	-	-
150	NCI0667935		8.5	0	54	65 ^f	-	-
151	NCI0368252		7.6	8.1	286	42 ^f	-	-

Table 5 (Continued)

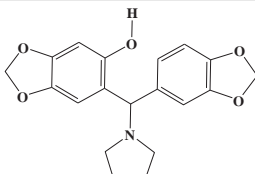
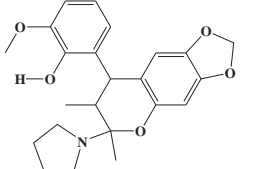
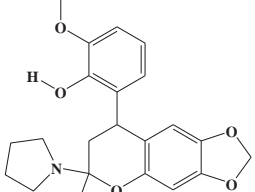
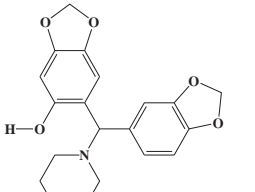
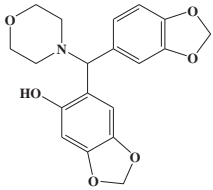
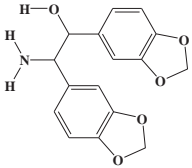
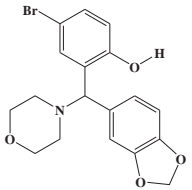
No. ^a	Name	Structure	Fit values ^b		QSAR Predictions ^c Ki (nM)	Experimental ^d		
			Hypoll/18/9	HypoV/31/5		% Inhibition at 100 μ M	IC ₅₀ (nM)	Ki (nM) ^e
152	NCI0370282		6.9	0	69	65 ^f	-	-
153	NCI0375504		8.4	0	69	80 ^{e,f}	45 $r^2=0.91^g$	17
154	NCI0375505		8.2	0	79	55 ^f	-	-
155	NCI0368254		7.3	0	96	51 ^f	-	-

Table 5 (Continued)

No. ^a	Name	Structure	Fit values ^b		QSAR Predictions ^c Ki (nM)	Experimental ^d		
			HypoIII/18/9	HypoV/31/5		% Inhibition at 100 μM	IC ₅₀ (nM)	Ki (nM) ^h
156	NCI0368248		7.4	0	103	30 ^f	-	-
157	NCI0132830		6.7	0	108	68 ^f	-	-
158	NCI0368263		7.2	0	113	73 ^{ef}	63 $r^2 = 0.87^g$	183

^a Compound numbers.

^b Best-fit values calculated by Eq. (D) in Section SM-1 under Supplementary Materials.

^c Predictions based on optimal QSAR equation (2).

^d Experimental in vitro activity against iNOS. Data represent the average of at least three trials.

^e Mass and ¹H NMR spectra of these compounds are shown in Supplementary Materials (Figs. D-I).

^f These compounds show >95% purities based on elemental (CHN) analysis. Table G in Supplementary Materials summarizes elemental analyses data and corresponding purities.

^g r^2 is the correlation coefficient of the dose-response curve (Figs. A-C under Supplementary Materials). Figs. B2 and B3, under Supplementary Materials, show the spectrophotometric recording of compound 145 at different concentrations (as example), and the difference in absorbance rate at 401 nm and 421 nm versus time, respectively [72].

^h Ki values were calculated from corresponding IC₅₀ values based on Cheng-Prusoff equation: $IC_{50} = Ki \left(1 + \frac{[S]}{Km} \right)$.

145: docking 145 into the binding pocket produced an interesting docked pose (Fig. 8C) reminiscent of the co-crystallized complex in Fig. 4 (PDB code: 3E7T, resolution 2.6 Å), whereby the halogenated aromatic ring is positioned at close proximity to the heme system, while the amino-ester alkyl chains protrudes toward Tyr341 allowing potential nucleophilic attack by the adjacent phenolic hydroxyl of Tyr341 against the activated hydrogen-bonded carboxylic carbonyl group of the ligand.

4. Conclusions

iNOS inhibitors are currently considered as potential treatments for several pathological conditions. The pharmacophoric space of iNOS inhibition was explored via seven diverse sets of inhibitors and using CATALYST-HYPOGEN to identify high quality binding model(s). Subsequently, genetic algorithm and multiple linear regression analysis were employed to access optimal QSAR model capable of explaining iNOS inhibitors bioactivity variation across 143 collected iNOS inhibitors. Two pharmacophoric models emerged in the QSAR equation suggesting the existence of at least two distinct binding modes accessible to ligands within iNOS binding pocket. The QSAR equation and the associated pharmacophoric models were experimentally validated by the identification of several iNOS inhibitors retrieved via in silico screening, out of which 3 illustrated nanomolar potencies: 145, 153 and 158. One of the inhibitors was found to inhibit iNOS irreversibly, probably through covalent bond formation. These results suggest that the combination of pharmacophoric exploration and QSAR analyses can be useful tool for finding new diverse iNOS inhibitors.

Acknowledgments

This project was sponsored by the Deanship of Scientific Research at the University of Jordan. The authors wish to thank the National Cancer Institute for freely providing hit compounds for experimental validation. The authors are also indebted to Prof. Richard B. Silverman for his invaluable advice and discussions.

Appendix A. Supplementary data

Supplementary data associated with this article can be found, in the online version, at <http://dx.doi.org/10.1016/j.jmgm.2012.04.001>.

References

- [1] J.F. Kerwin, M. Heller, The arginine–nitric oxide pathway: a target for new drugs, *Med. Res. Rev.* 14 (1994) 23–74.
- [2] L.J. Roman, P. Martásek, B.S.S. Masters, Intrinsic and extrinsic modulation of nitric oxide synthase activity, *Chem. Rev.* 102 (2002) 1179–1190.
- [3] C.S. Raman, P.H.Y. Martasek, V. Kral, B.S.S. Masters, T.L. Poulos, Crystal structure of constitutive endothelial nitric oxide synthase: a paradigm for pterin function involving a novel metal center, *Cell* 95 (1998) 939–950.
- [4] D.A. Wink, J.B. Mitchell, Chemical biology of nitric oxide: insights into regulatory, cytotoxic, and cytoprotective mechanisms of nitric oxide, *Free Radical Biol. Med.* 25 (1998) 434–456.
- [5] P. Pacher, J.S. Beckman, L. Liaudet, Nitric oxide and peroxynitrite in health and disease, *Physiol. Rev.* 87 (2007) 315–424.
- [6] Z.Q. Liu, S.M. Wildhirt, H.H. Zhou, Specificity of inducible nitric-oxide synthase inhibitors: prospects for their clinical therapy, *Acta Pharmacol. Sin.* 20 (1999) 1052–1056.
- [7] D.S. Bredt, S.H. Snyder, Nitric-oxide – a physiological messenger molecule, *Annu. Rev. Biochem.* 63 (1994) 175–195.
- [8] R.M.J. Palmer, A.G. Ferrige, S. Moncada, Nitric oxide release accounts for the biological activity of endothelium-derived relaxing factor, *Nature* 327 (1987) 524–526.
- [9] J.T. Groves, C.C.Y. Wang, Nitric oxide synthase: models and mechanisms, *Curr. Opin. Chem. Biol.* 4 (2000) 687–695.
- [10] F. Aktan, iNOS-mediated nitric oxide production and its regulation, *Life Sci.* 75 (2004) 639–653.
- [11] K.D. Kroncke, K. Fehsel, V. Kolb-Bachofen, Inducible nitric oxide synthase in human diseases, *Clin. Exp. Immunol.* 113 (1998) 147–156.
- [12] Q.W. Ma, Zheng, Zhang, Min, Hu, Hengtong, Li, Junhui, Zhang, Dong, Guo, Kun, Sha, Huanchen, Targeting the L-arginine–nitric oxide pathway for cancer treatment, *Curr. Pharm. Design.* 16 (2010) 392–410.
- [13] W.K. Alderton, C.E. Cooper, R.G. Knowles, Nitric oxide synthases: structure, function and inhibition, *Biochem. J.* 357 (2001) 593–615.
- [14] S. Connolly, A. Aberg, A. Arvai, H.G. Beaton, D.R. Cheshire, A.R. Cook, S. Cooper, D. Cox, P. Hamley, P. Mallinder, I. Millichip, D.J. Nicholls, R.J. Rosenfeld, S.A. St-Gallay, J. Tainer, A.C. Tinker, A.V. Wallace, 2-Aminopyridines as highly selective inducible nitric oxide synthase inhibitors. Differential binding modes dependent on nitrogen substitution, *J. Med. Chem.* 47 (2004) 3320–3323.
- [15] A.C. Tinker, H.G. Beaton, N. Boughton-Smith, T.R. Cook, S.L. Cooper, L. Fraser-Rae, K. Hallam, P. Hamley, T. McNally, D.J. Nicholls, A.D. Pimm, A.V. Wallace, 1,2-Dihydro-4-quinazolinamines: potent, highly selective inhibitors of inducible nitric oxide synthase which show antiinflammatory activity in vivo, *J. Med. Chem.* 46 (2003) 913–916.
- [16] M. Whitlow, M. Adler, D. Davey, Q. Huang, S. Koovakkat, J.F. Parkinson, E. Pham, M. Polokoff, W. Xu, S. Yuan, G. Phillips, The rational design of inhibitors of nitric oxide formation by inducible nitric oxide synthase, *Bioorg. Med. Chem. Lett.* 17 (2007) 2505–2508.
- [17] D.D. Davey, M. Adler, D. Arnaiz, K. Eagen, S. Erickson, W. Guilford, M. Kenrick, M.M. Morrissey, M. Ohlmeyer, G. Pan, V.M. Paradar, J. Parkinson, M. Polokoff, K. Saionz, C. Santos, B. Subramanyam, R. Vergona, R.G. Wei, M. Whitlow, B. Ye, Z. Zhao, J.J. Devlin, G. Phillips, Design, synthesis, and activity of 2-imidazol-1-ylpyrimidine derived inducible nitric oxide synthase dimerization inhibitors, *J. Med. Chem.* 50 (2007) 1146–1157.
- [18] G.A.R.Y. Suaifan, C.L. Goodyear, M.D. Threadgill, Synthesis of N(methoxycarbonylthienylmethyl). Thioureas and evaluation of their interaction with inducible and neuronal nitric oxide synthase, *Molecules* 15 (2010) 3121–3134.
- [19] H. Ji, J.A. Gómez-Vidal, P. Martásek, L.J. Roman, R.B. Silverman, Conformationally restricted dipeptide amides as potent and selective neuronal nitric oxide synthase inhibitors, *J. Med. Chem.* 49 (2006) 6254–6263.
- [20] J. Seo, P. Martasek, L.J. Roman, R.B. Silverman, Selective L-nitroargininylaminopyrrolidine and L-nitroargininylaminopiperidine neuronal nitric oxide synthase inhibitors, *Bioorg. Med. Chem.* 15 (2007) 1928–1938.
- [21] E.D. Garcin, A.S. Arvai, R.J. Rosenfeld, M.D. Kroeger, B.R. Crane, G. Andersson, G. Andrews, P.J. Hamley, P.R. Mallinder, D.J. Nicholls, S.A. St-Gallay, A.C. Tinker, N.P. Gensmantel, A. Mete, D.R. Cheshire, S. Connolly, D.J. Stuehr, A. Aberg, A.V. Wallace, J.A. Tainer, E.D. Getzoff, Anchored plasticity opens doors for selective inhibitor design in nitric oxide synthase, *Nat. Chem. Biol.* 4 (2008) 700–707.
- [22] K. McMillan, M. Adler, D.S. Auld, J.J. Baldwin, E. Blasko, L.J. Browne, D. Chelsky, D. Davey, R.E. Dolle, K.A. Eagen, S. Erickson, R.I. Feldman, C.B. Glaser, C. Mallari, M.M. Morrissey, M.H. Ohlmeyer, G. Pan, J.F. Parkinson, G.B. Phillips, M.A. Polokoff, N.H. Sigal, R. Vergona, M. Whitlow, T.A. Young, J.J. Devlin, Allosteric inhibitors of inducible nitric oxide synthase dimerization discovered via combinatorial chemistry, *Proc. Natl. Acad. Sci. U.S.A.* 97 (2000) 1506–1511.
- [23] N.R.A. Beeley, C. Sage, GPCRs: an update on structural approaches to drug discovery, *Targets* 2 (2003) 19–25.
- [24] H. Steuber, M. Zentgraf, C. Gerlach, C.A. Sotriffer, A. Heine, G. Klebe, Expect the unexpected or caveat for drug designers: multiple structure determinations using aldose reductase crystals treated under varying soaking and co-crystallisation conditions, *J. Mol. Biol.* 363 (2006) 174–187.
- [25] M.T. Stubbs, S. Reyda, F. Dullweber, M. Moller, G. Klebe, D. Dorsch, W. Mederski, H. Wurziger, pH-dependent binding modes observed in trypsin crystals: lessons for structure-based drug design, *Chem. Biochem. J.* 3 (2002) 246–249.
- [26] G. Klebe, Virtual ligand screening: strategies, perspectives and limitations, *Drug Discov. Today* 11 (2006) 580–594.
- [27] M.A. DePristo, P.I.W. de Bakker, T.L. Blundell, Heterogeneity and inaccuracy in protein structures solved by X-ray crystallography, *Structure* 12 (2004) 831–838.
- [28] V. Aparna, G.R. Desiraju, B. Gopalakrishnan, Insights into ligand selectivity in nitric oxide synthase isoforms: a molecular dynamics study, *J. Mol. Graph. Model.* 26 (2007) 457–470.
- [29] M.O. Taha, Y. Bustanji, M.A.S. Al-Ghoussein, M. Mohammad, H. Zalloum, I.M. Al-Masri, N. Atallah, Pharmacophore modeling, quantitative structure–activity relationship analysis, and in silico screening reveal potent glycogen synthase kinase-3 β inhibitory activities for cimetidine, hydroxychloroquine, and gemifloxacin, *J. Med. Chem.* 51 (2008) 2062–2077.
- [30] M.O. Taha, N. Atallah, A.G. Al-Bakri, C. Paradis-Bleau, H. Zalloum, K.S. Younis, R.C. Levesque, Discovery of new MurF inhibitors via pharmacophore modeling and QSAR analysis followed by in-silico screening, *Bioorg. Med. Chem.* 16 (2008) 1218–1235.
- [31] M.O. Taha, Y. Bustanji, A.G. Al-Bakri, A.-M. Yousef, W.A. Zalloum, I.M. Al-Masri, N. Atallah, Discovery of new potent human protein tyrosine phosphatase inhibitors via pharmacophore and QSAR analysis followed by in silico screening, *J. Mol. Graph. Model.* 25 (2007) 870–884.
- [32] I.M. Al-masri, M.K. Mohammad, M.O. Taha, Discovery of DPP IV inhibitors by pharmacophore modeling and QSAR analysis followed by in silico screening, *Chem. Med. Chem.* 3 (2008) 1763–1779.
- [33] M.O. Taha, L.A. Dahabiyeh, Y. Bustanji, H. Zalloum, S. Saleh, Combining ligand-based pharmacophore modeling, quantitative structure–activity relationship analysis and in silico screening for the discovery of new potent hormone sensitive lipase inhibitors, *J. Med. Chem.* 51 (2008) 6478–6494.

- [34] A. Al-Nadaf, G.A. Sheikha, M.O. Taha, Elaborate ligand-based pharmacophore exploration and QSAR analysis guide the synthesis of novel pyridinium-based potent [beta]-secretase inhibitory leads, *Bioorg. Med. Chem.* 18 (2010) 3088–3115.
- [35] A.M. Abu Hammad, M.O. Taha, Pharmacophore modeling, quantitative structure–activity relationship analysis, and shape-complemented in silico screening allow access to novel influenza neuraminidase inhibitors, *J. Chem. Inf. Model.* 49 (2009) 978–996.
- [36] R. Abu Khalaf, G. Abu Sheikha, Y. Bustanji, M.O. Taha, Discovery of new cholesteryl ester transfer protein inhibitors via ligand-based pharmacophore modeling and QSAR analysis followed by synthetic exploration, *Eur. J. Med. Chem.* 45 (2010) 1598–1617.
- [37] M.A. Al-Sha'er, M.O. Taha, Discovery of novel CDK1 inhibitors by combining pharmacophore modeling, QSAR analysis and in silico screening followed by in vitro bioassay, *Eur. J. Med. Chem.* 45 (2010) 4316–4330.
- [38] M.A. Al-Sha'er, M.O. Taha, Elaborate ligand-based modeling reveals new nanomolar heat shock protein 90 α inhibitors, *J. Chem. Inf. Model.* 50 (2010) 1706–1723.
- [39] CATALYST 4.11 Users' Manual, Accelrys Software Inc., San Diego, CA, 2005.
- [40] R.B. Silverman, H. Huang, M.A. Marletta, P. Martasek, Selective inhibition of neuronal nitric oxide synthase by N-omega-nitroarginine- and phenylalanine-containing dipeptides and dipeptide esters, *J. Med. Chem.* 40 (1997) 2813–2817.
- [41] H.Q. Zhang, W. Fast, M.A. Marletta, P. Martasek, R.B. Silverman, Potent and selective inhibition of neuronal nitric oxide synthase by N-omega-propyl-L-arginine, *J. Med. Chem.* 40 (1997) 3869–3870.
- [42] H. Huang, P. Martasek, L.J. Roman, B.S.S. Masters, R.B. Silverman, N-omega-nitroarginine-containing dipeptide amides. Potent and highly selective inhibitors of neuronal nitric oxide synthase, *J. Med. Chem.* 42 (1999) 3147–3153.
- [43] Y. Lee, P. Martasek, L.J. Roman, B.S.S. Masters, R.B. Silverman, Imidazole-containing amino acids as selective inhibitors of nitric oxide synthases, *Bioorg. Med. Chem.* 7 (1999) 1941–1951.
- [44] H. Huang, P. Martasek, L.J. Roman, R.B. Silverman, Synthesis and evaluation of peptidomimetics as selective inhibitors and active site probes of nitric oxide synthases, *J. Med. Chem.* 43 (2000) 2938–2945.
- [45] Y. Lee, P. Martasek, L.J. Roman, R.B. Silverman, 1H-pyrazole-1-carboxamides: new inhibitors of nitric oxide synthase, *Bioorg. Med. Chem. Lett.* 10 (2000) 2771–2774.
- [46] J.M. Hah, P. Martasek, L.J. Roman, R.B. Silverman, Aromatic reduced amide bond peptidomimetics as selective inhibitors of neuronal nitric oxide synthase, *J. Med. Chem.* 46 (2003) 1661–1669.
- [47] H.T. Ji, H.Y. Li, M. Flinspach, T.L. Poulos, R.B. Silverman, Computer modeling of selective regions in the active site of nitric oxide synthases: implication for the design of isoform-selective inhibitors, *J. Med. Chem.* 46 (2003) 5700–5711.
- [48] Y. Zhu, D. Nikolic, R.B. Van Breemen, R.B. Silverman, Mechanism of inactivation of inducible nitric oxide synthase by amidines. Irreversible enzyme inactivation without inactivator modification, *J. Am. Chem. Soc.* 127 (2004) 858–868.
- [49] B.N.A. Mbadugha, J. Seo, H. Ji, P. Martasek, L.J. Roman, T.M. Shea, H. Li, T.L. Poulos, R.B. Silverman, Hydroxyl-terminated peptidomimetic inhibitors of neuronal nitric oxide synthase, *Bioorg. Med. Chem.* 14 (2006) 3681–3690.
- [50] H. Ji, B.Z. Stanton, J. Igarashi, H. Li, P. Martasek, L.J. Roman, T.L. Poulos, R.B. Silverman, Minimal pharmacophoric elements and fragment hopping, an approach directed at molecular diversity and isozyme selectivity design of selective neuronal nitric oxide synthase inhibitors, *J. Am. Chem. Soc.* 130 (2008) 3900–3914.
- [51] H.T. Ji, H.Y. Li, P. Martasek, L.J. Roman, T.L. Poulos, R.B. Silverman, Discovery of highly potent and selective inhibitors of neuronal nitric oxide synthase by fragment hopping, *J. Med. Chem.* 52 (2009) 779–797.
- [52] J. Seo, J. Igarashi, H. Li, P. Martasek, L.J. Roman, T.L. Poulos, R.B. Silverman, Structure-based design and synthesis of N(omega)-nitro-L-arginine-containing peptidomimetics as selective inhibitors of neuronal nitric oxide synthase. Displacement of the heme structural water, *J. Med. Chem.* 50 (2007) 2089–2099.
- [53] H. Li, J. Sutter, R. Hoffmann, in: O.F. Güner (Ed.), *Pharmacophore Perception, Development, and Use in Drug Design*, International University Line, California, 2000, pp. 173–189.
- [54] J. Sutter, O. Güner, R. Hoffmann, H. Li, M. Waldman, *Effect of Variable Weights and Tolerances on Predictive Model Generation*. *Pharmacophore Perception, Development and Use in Drug Design*, International University Line, California, 2000, pp. 501–511.
- [55] Y. Kurogi, O.F. Güner, *Pharmacophore modeling and three-dimensional database searching for drug design using catalyst*, *Curr. Med. Chem.* 8 (2001) 1035–1055.
- [56] *Discovery Studio 2.5.5 User Guide*, Accelrys Inc., San Diego, CA, 2010.
- [57] R. Fisher, *The Principle of Experimentation Illustrated by a Psycho-physical ExpeHafner Publishing Co., eighth ed., Hafner Publishing, New York, 1966 (Chapter II)*.
- [58] E.M. Krovat, T. Langer, Non-peptide angiotensin ii receptor antagonists: chemical feature based pharmacophore identification, *J. Med. Chem.* 46 (2003) 716–726.
- [59] CERIU2, QSAR Users' Manual, Version 4.10, Accelrys Inc., San Diego, CA, 2005, pp. 43–88, 221–235, 237–250.
- [60] C.A. Lipinski, F. Lombardo, B.W. Dominy, P.J. Feeney, Experimental and computational approaches to estimate solubility and permeability in drug discovery and development settings, *Adv. Drug Deliv. Rev.* 46 (2001) 3–26.
- [61] D.F. Veber, S.R. Johnson, H.-Y. Cheng, B.R. Smith, K.W. Ward, K.D. Kopple, Molecular properties that influence the oral bioavailability of drug candidates, *J. Med. Chem.* 45 (2002) 2615–2623.
- [62] J.M. Hevel, K.A. White, M.A. Marletta, Purification of the inducible murine macrophage nitric oxide synthase. Identification as a flavoprotein, *J. Biol. Chem.* 266 (1991) 22789–22791.
- [63] L.F. Ramsey, W.D. Schafer, *The Statistical Sleuth*, first ed., Wadsworth Publishing Company, USA, 1997.
- [64] M.L. Verdonk, V. Berdini, M.J. Hartshorn, W.T.M. Mooij, C.W. Murray, R.D. Taylor, P. Watson, Virtual screening using protein–ligand docking: avoiding artificial enrichment, *J. Chem. Inf. Comput. Sci.* 44 (2004) 793–806.
- [65] J. Kirchmair, P. Markt, S. Distinto, G. Wolber, T. Langer, Evaluation of the performance of 3D virtual screening protocols: RMSD comparisons, enrichment assessments, and decoy selection—what can we learn from earlier mistakes? *J. Comput. Aid. Mol. Des.* 22 (2008) 213–228.
- [66] J.J. Irwin, B.K. Shoichet, Zinc—a free database of commercially available compounds for virtual screening, *J. Chem. Inf. Model.* 45 (2004) 177–182.
- [67] N. Triballeau, F. Acher, I. Brabet, J.-P. Pin, H.-O. Bertrand, Virtual screening workflow development guided by the “receiver operating characteristic” curve approach. application to high-throughput docking on metabotropic glutamate receptor subtype 4, *J. Med. Chem.* 48 (2005) 2534–2547.
- [68] M. Jacobsson, P. Lidén, E. Stjernschantz, H. Boström, U. Norinder, Improving structure-based virtual screening by multivariate analysis of scoring data, *J. Med. Chem.* 46 (2003) 5781–5789.
- [69] S. Ulhaq, E.C. Chinje, M.A. Naylor, M. Jaffar, I.J. Stratford, M.D. Threadgill, Heterocyclic analogues of -citrulline as inhibitors of the isoforms of nitric oxide synthase (NOS) and identification of N[delta]-(4,5-dihydrothiazol-2-yl)ornithine as a potent inhibitor, *Bioorg. Med. Chem.* 7 (1999) 1787–1796.
- [70] P.A. Lanzetta, L.J. Alvarez, P.S. Reinach, O.A. Candia, An improved assay for nanomole amounts of inorganic phosphate, *Anal. Biochem.* 100 (1979) 95–97.
- [71] C. Avila, B.A. Kornilayev, B.S.J. Blagg, Development and optimization of a useful assay for determining Hsp90s inherent ATPase activity, *Bioorg. Med. Chem.* 14 (2006) 1134–1142.
- [72] J. Joubert, S. van Dyk, S.F. Malan, Fluorescent polycyclic ligands for nitric oxide synthase (NOS) inhibition, *Bioorg. Med. Chem.* 16 (2008) 8952–8958.